

## CHAPTER 6

---

# CALORIMETRY

---

### 6.1 Introduction to calorimeters

Calorimeters of the CEPC detector, including electromagnetic calorimeter (ECAL) and hadron calorimeter (HCAL), are employed for precise energy measurements of electron, photon, tau and hadronic jets. To fully exploit the physics potential about Higgs, W, Z and related SM processes, the jet energy resolution  $\sigma_E/E$  is required to reach 3%-4%, or  $30\%/\sqrt{E}$  at energies below about 100 GeV. This resolution is about a factor of two smaller than the calorimeters used for the LEP detectors and currently operating calorimeters at the LHC. It significantly improves the separation of the W and Z bosons which decay into two jets, as shown in Figure 6.1. The basic requirements for ECAL and HCAL resolution are  $16\%/\sqrt{E}$  and  $50\%/\sqrt{E}$ , respectively.

To achieve the required jet energy resolution, many R&D researches are carried out within the CALICE collaboration since 2000 [1]. The majority of these studies aim to develop extremely fine granularity and compact imaging calorimeters with several technology options shown in Figure 6.2. Imaging calorimeter is a rapidly developing novel particle detector which has excellent spatial resolution. It is capable to provide enormous position information of incident and showering particles, which makes it possible to reconstruct every single particle cluster. This is vital for Particle Flow Algorithm (PFA [2]) and help to significantly improve the energy resolution of hadrons. The basic idea of PFA is to distinguish charged ( $\sim 65\%$ ) and neutral particles ( $\sim 35\%$ ) inside the calorimeters. Charged particles measured in the inner tracker with high momentum resolution are matched to their energy depositions in the calorimeters. Energy depositions without matched inner tracks are considered to originate from neutral particles inside jets, among

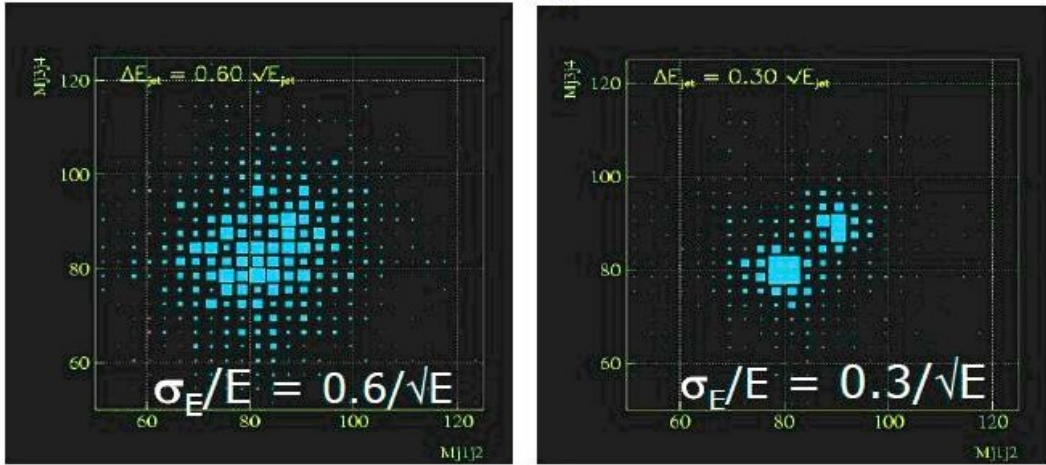


**Figure 6.1:** Separation of W and Z bosons with different jet energy resolutions.

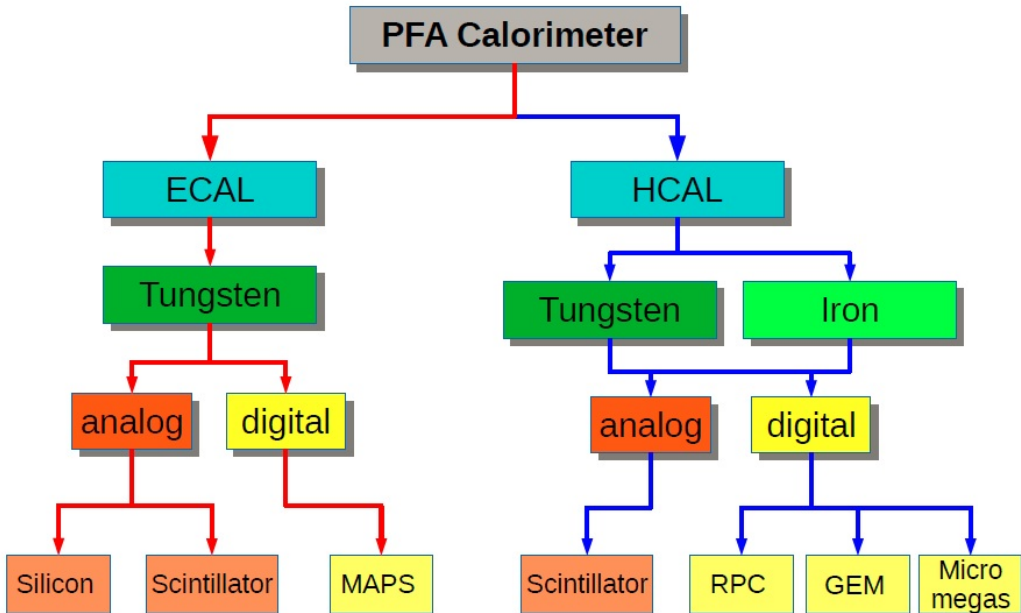


**Figure 6.2:** PFA: Imaging calorimeters being developed by the CALICE collaboration since 2000.

these neutral particles, about 25% of energy from photons are measured in the ECAL with good energy resolution, while the residual energy of merely 10% from neutral hadrons are measured by the calorimeters with poor energy resolution. Hence, the jet energy is determined by the charged track momenta of charged particles from inner tracker and energy depositions of neutral particles in the calorimeters. It has been demonstrated that significant improvement of the jet energy resolution is achievable based on MC simulations and test beam measurements. However, more efforts are needed to optimize the calorimeter design, to improve the PFA, and to develop the technologies for high granularity imaging calorimeters.

The calorimeter system includes two sub-detectors, an electromagnetic calorimeter (ECAL) which is optimized for the measurement of photons and electrons, and a hadronic

calorimeter (HCAL) which is employed to measure the energy deposit of the hadronic showers caused by the hadronic particles when they are absorbed in the HCAL detector. The two sub-detectors will be installed within the solenoid to minimize the inactive material in front of the calorimeters and to reliably associate tracks to energy deposits. The calorimeter system is divided into three parts, one cylindrical barrel and two end-caps.

The ECAL consists of layers of active sensors (such as silicon pads or pixels, or scintillator detector) interleaved with absorber tungsten plates. The digital HCAL (DHCAL) is expected to have stainless steel absorber plates with gaseous detectors such as glass Resistive Plate Chambers (gRPC) or GEM, or analog HCAL (AHCAL) using scintillator with SiPM readout as sensor. Both ECAL and HCAL are sampling detectors with very fine granularity and segmentations of electronic readout which is driven by excellent separations requirement between charged and neutral particles for the particle flow algorithms.

From Figure 6.2, there are more detector options with enormous worldwide R&D efforts ongoing within the CALICE collaboration. Another approach for high performance calorimeters is dual-readout calorimetry.

However, for this particular CDR, we have to be selective and focus on a few options with collaborators who expressed great interests so far. The CEPC detectors R&D is widely open for international collaboration with different detector options and new ideas.

## 6.2 Electromagnetic Calorimeter for Particle Flow Approach

The particle flow paradigm has tremendous impact on the design of the electromagnetic calorimeter detector. Separating overlap showers from each other is principal requirement of the detector. A calorimeter used for particle flow thus needs to be able to do pattern recognition in the shower. The electromagnetic section has lots of tasks to fulfill. It should be able to select photons from close-by particles. It should be able to reconstruct the detailed properties of the shower, such as shower shape, starting point and energy distribution. It should be able to distinguish early starting electromagnetic showers from hadronic ones. The imaging capabilities of the calorimeter are more important than the intrinsic single particle energy resolution, although the latter is still important to the particle flow performance for electron, photons and jets. Due to the reason that about half of the hadronic showers will start development inside the electromagnetic calorimeter, a calorimeter with excellent three dimensional granularity is of utmost importance. In order to have the ability of separate close-by showers in the calorimeter, the detector with small Moliere radius is required. A large ratio between interaction length and radiation length of the detector is advantageous to the separation between electromagnetic and hadronic showers. A small radiation length will make the start of the electromagnetic shower earlier in the calorimeter, while a large interaction length will reduce the fraction of hadronic showers starting in the calorimeter. At the same time, the calorimeter with a compact structure is favorable.

In this section, we focus on two detector options for the ECAL, which consist of layers of active sensors (silicon pads or pixels, or scintillator detector) interleaved with absorber tungsten plates.

## 6.2.1 Silicon-Tungsten Sandwich Electromagnetic Calorimeter

### 6.2.1.1 Introduction

The study of the Higgs is not the only goal of a machine at 250 centre-of-mass energy. It can be generalised to the multi boson physics (Z, W and H). The best way to use the excellent luminosity foreseen at CEPC, consist to tag the boson through their mass in their decays into  $q\bar{q}$  (2 jets). Taking into account the natural width of the Z and W, it has been shown that this goal required to achieve a jet energy resolution of  $30\%/\sqrt{E_{\text{Jet}}}$ , thus a factor two better than the energy resolution achieved for a typical detector at LEP.

It has been shown [3] that a method consisting to fully reconstruct every single particle could reach this goal (Particle Flow Algorithm); it requires both a high performance tracker, typically achieving  $\delta p/p$  of  $10^5 p/GeV$  associated with high granularity calorimeters able to separate the contribution from individual particles down to the MIP level. As a typical jet is contains fractions in energy of 65%, 25% and 10% of charged particles, photons and neutral hadrons respectively, a moderate calorimetric resolution is then sufficient to achieve the goal. In this framework, the electromagnetic calorimeter (ECal), is first devoted to measure photon(s) and to a lesser extent electron(s) and to make a full pattern of the deposited energy of the hadron, i.e. shower of hadron interacting in the ECAL. To avoid “blind region”, the entire calorimeter has to be put inside the super-conductive solenoid. The compactness is therefore an important criterion.

The design of the calorimeters have to take the following guidelines into account [4]:

- Optimisation of the number of calorimeter cells (cell size and number of layers)
- Choice of the absorber material in order to insure a high level of compactness and the infra-structural components such as cooling, power supplies, readout cables and the very front end electronics.

For the electromagnetic calorimeter these criteria has led to the choice of Tungsten with a radiation length of  $X_0=3.5\text{mm}$ , a Moli?re radius of  $RM=9\text{mm}$  and an interaction length of  $\lambda_I = 96\text{mm}$ .

### 6.2.1.2 Silicon sensors

Among several sensor techniques, high resistivity silicon pin diodes offer several unique intrinsic advantages:

- stability: under a reasonable bias voltage, completely depleted pin-diode have a gain of one, and a signal response to MIP mostly defined by the thickness of the sensor, with a very low dependence on temperature, radiation, humidity, ...
- uniformity: for the same reason, the control of the thickness over large batches (typically to less than a percent) ensures a uniformity of response within a wafer and between them. The nonsensitive area between wafers has recently been reduced by the use of laser cutting, thinned guard-ring design [5], and would benefit from the use of larger ingot size (8” becoming the standard).
- flexibility: the dimension and geometry of the cells are defined by the readout pad on the PCB.

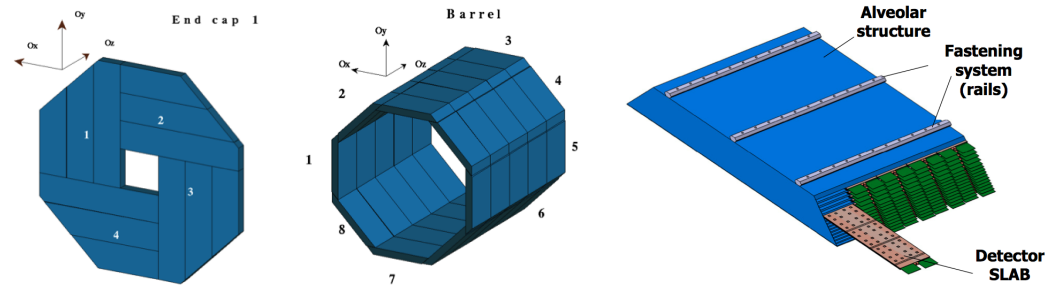


**Figure 6.3:** Left: Geometry of the SiW-ECAL Endcaps. Middle: Barrel Right: Geometry of the barrel modules.

- High Signal-to-Noise ratio: with  $\simeq 80$  electron-hole pairs created by linear mm of MIP track, MIPs tracks can easily be traced in the calorimeters, which is critical for the god performance of

The only real drawback of Silicon sensors remaining is their price, to be expected around  $2 - 3\$/cm^2$ .

By associating of Silicon sensors with Tungsten absorbers and Carbon Fibre structures, the SiW-ECAL offers an excellent option for PFA optimised calorimetry.

#### 6.2.1.3 Constraints

High granularity calorimetry, and ECal especially, is technically challenging: the very number of channels calls for an embedded readout and zero suppression, to limits the amount of connections; in turn embedded readout power consumption should be as limited as possible to avoid large cooling systems which would degrade the capacity of the calorimeter. In the best case the cooling should stay passive at the heart of the calorimeters.

The design proposed for the CEPC SiW-ECal is very largely inspired by the one of the ILD detector for ILC as described in the Detector baseline Document [6]; it is influenced by the options studied for the CMS High-Luminosity upgrade endcap replacement HG-CAL [7, 8], concerning cooling and electronics. In terms of luminosity and collision rates, the CEPC lies between the 2 options.

#### 6.2.1.4 Mechanics & design

The geometry presented here reflects the current (october 2017) status on the realistic models developed for ILD. It differs slightly from the CEPC\_v1 and CEPC\_v4 models [9], mainly on ECAL thickness (223mm vs 185mm), and inner radius of the endcaps (226.8 and 245mm vs 400mm).

#### 6.2.1.5 Geometry

The geometry of the detector is based on ILD detector, where there is no blind zone between modules, but only “special zone”, where it has been shown that performance of the reconstruction of jets or photon(s) is not downgraded significantly [10].

The figure below shows this octagonal geometry and the possible way to build the detector:

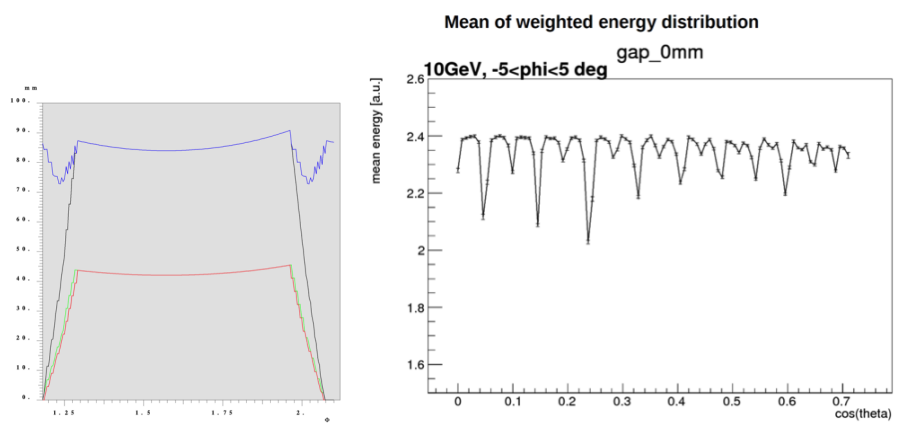


**Figure 6.4:** Left: Thickness of Tungsten seen as function of the polar azimuthal angle scan of one octant of the barrel. Right: Mean Theta angle scan

**Ecal thickness** For a baseline design featuring 30 layers – split in 2 sections of 20 and 10 layers, holding each an equal amount of  $12X_0$  of W – 525 microns thick wafers, and a base plate of 20mm of carbon, the ECal thickness is estimated at 223mm.

For a reduced number of layers, at 22 (with section of 14 and 8), but thicker wafers (725 microns), the thickness becomes 191mm.

**Ecal dimensions** The Barrel consist of 8 staves of 5 trapezoidal modules. Each barrel module contains 5 columns of alveoli. The number of modules and alveoli is even in order to avoid any special region at the azimuthal angle  $\theta = 0$ . The alveolus size is fixed to 186mm by mechanical limits and by cost optimisation considerations, to contain exactly two 6-inch wafers or one-and-a-half 8-inch wafer. Integrating the alveolus size, walls of modules and contingencies, the barrel length amount to 4700mm. (4900mm in CEPC simulations). A gap of typically 70mm (100mm in simulation) is left between the barrel sides and end-cap front parts, whose precise dimension will depend on the amount of ancillaries needed to service the ECAL and trackers (power and DAQ cables, cooling pipes, patch panels).

The end-caps are made of quadrants of 2 modules of 4 and 3 alveoli columns. Their inner radius is fixed by the ECal ring at 400mm. With 7 alveoli columns, the end-cap outer radius is 1755mm. An overshoot of 32mm is left between the outer radius of the barrel and of the end-caps, in order to contain the EM shower impinging the region of overlap. see figure 6.4. This fixes the inner radius size of the ECal barrel at 1498mm or 1530mm.

For such a geometry, summing the barrel (200) and end-caps (56), 256 alveoli columns are needed. For 22 (resp. 30) layers, and this yields 5632 (7680) alveoli, and as many detector slabs.

**Slab geometry** In each alveola of the modules, a slab is inserted. Slabs contains 2 symmetric layers of Silicon sensors glued on PCB, equipped with readout ASICs, high voltage distribution by a Kapton foil and copper layers for passive cooling. The elements are chained on both sides of a Carbon fibre cradle taking the shape of an H, with a core of Tungsten, and shielded by an aluminium cover. This so-called H-Structure is illustrated below.

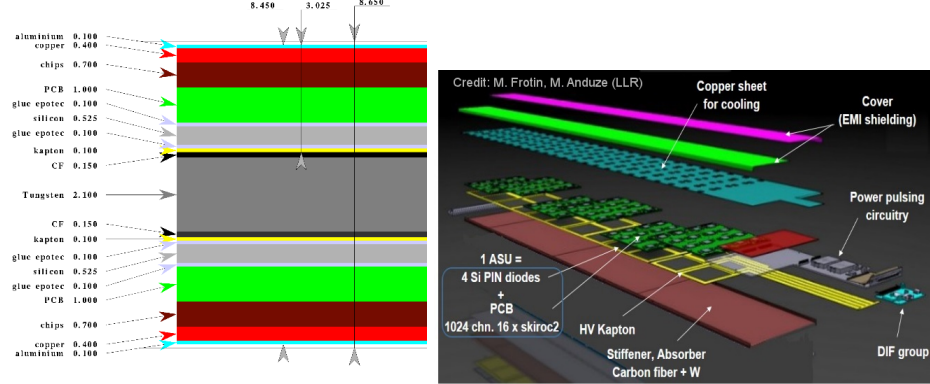


**Figure 6.5:** Left: Transverse cut through a thin layer of the SLAB. Right: Exploded view of the top layer of a slab of the SiW-ECAL. The same structure is mirrored below the slab.

To insure scalability and industrial production, the design has been made as modular as possible: the basic unit is the ASU (Assembly Single Unit), made of a  $18 \times 18 \text{ mm}^2$  PCB onto which 4 wafers of  $90 \times 90 \text{ mm}^2$  wafers are glued. Each ASU would handle 256 cells with 4 ASICs, for cell surfaces of  $11.25 \times 11.25 \text{ mm}^2$ .

The ASUs are chained together for the clock and configuration distribution and data collection. For a radius of  $1498 \text{ mm}$  the longest (shortest) barrel slabs measure  $1146 \text{ mm}$  ( $955 \text{ mm}$ ).

### 6.2.1.6 Electronics

One of the most critical element of the CEPC calorimeters is the readout electronics which is defined by the dynamic range, the effective digitisation, mode of trigger, the rate of working and power consumption per channel.

**Dynamic range:** A MIP going through a  $725 \mu\text{m}$  diode would produce  $\simeq 60000$  electron-pairs holes or a charge of  $9.6 \text{ fC}$  as the most probable value (MPV). To record MIPs with an efficiency higher than 95% this ports the low-end of the dynamic range to a 1/3 of the MPV. The high-end is determined by the number of MIP equivalent at the core of the high-energy EM showers, which can reach up-to 10000 MPV or  $96 \text{ pC}$  for  $11 \times 11 \text{ mm}^2$  cells.

**Timing:** Time measurement of deposits in the calorimeters can be useful to Particle Flow algorithms to help disambiguate particle contributions. For the CMS HGCAL it is planned to distinguish particle stemming from different interactions [7], by achieving a timing of  $50 - 20 \text{ ps}$  on EM showers. For  $e^+e^-$  colliders, with a single primary vertex, precision timing of individual cells – or group of cells – could still be useful to reduced the confusion and improve the resolution. The required precision is uncertain and should be studied further. Recent version of the SKYROC2a ASIC, could be operated [11] on test board with a measure of time close to  $1.4 \text{ ns}$ . The performance has to be measured in an integrated design.

**Rates:** The running conditions a circular collider preclude any pulsed operation as is planned for the linear ones, where clocks, pre-amps, digital conversion are powered sequentially at a few Hz. A partial in-time shut-off or local on-demand switch-on of the ADC and TDC parts can be envisaged, leaving the pre-amp as the single major power

consumer. As a point of reference, the current power consumption for SKIROC2 chips designed for the SiW-ECAL of ILD is of  $5\text{mW}$  per channel in continuous mode.

**Occupancy:** The occupancy of the calorimeters should be very low. This pushes in the direction of designing pre-amps with a very small consumption when there is no signal.

### 6.2.1.7 Power & Cooling

To the first order, the amount of power dissipates scales with the number of electronics channels. One important issue is to decide on the power scheme:

- a reduced number of channels using only passive cooling at the heart of the detector, such as planned at the ILD; a  $400\text{microns}$ -thick copper sheet will drain the heat to the end of the slab, where it is removed by a cooling system.
- keep a high granularity but include  $\text{CO}_2$  cooling in the absorbers such as envisaged for the HGCAL.

The CEPC ECAL is at edge of both options, with a limit for the purely passive option of the order of  $2x2\text{cm}^2$  cells for a increase of temperature limited to  $\Delta T \sim 10^\circ\text{C}$  at the remote-end of the slab.

**Water cooling** Current plans for the ILD SiW-ECAL is to use a leak-less water cooling system to extract the heat at the end of each slab from the copper. Details of implementation can be found in [12? ].

**$\text{CO}_2$  cooling** HGCAL is preparing a biphasic  $\text{CO}_2$  cooling system, with pipes circulating inside the absorber planes, made of an alloy of Tungsten and Copper.

A similar system adapted to the SiW-ECAL has been simulated [13]. The ILD  $400\text{microns}$  passive colling are replaced by plates of  $3\text{mm}$  of Copper, equipped with  $1.6\text{mm}$  inner-diameter pipes for  $\text{CO}_2$  circulation, glued on the ASICs, on both side of the slab. Assuming a fully transversally isolated system, with ASICs a sole heat source at equilibrium dissipating  $0.64\text{W}$  ( $10\text{mW}$  per channel times 64 channels), and a fixed working point of  $20^\circ\text{C}$  for  $\text{CO}_2$  (i.e assuming perfect heat absorption), a doubled sided module of  $252x252\text{mm}^2$  holding 32 chips cooled by  $2x2$  pipes was simulated.

Very preliminary simulations in "ideal conditions" show a difference of  $\Delta T \sim 2^\circ\text{C}$  mostly centered on ASIC's ( $0.3^\circ\text{C}$  in the exchanger itself only).

### 6.2.1.8 Status of R&D

The performances of a Silicon-Tungsten ECAL have beed explored using the "physical prototype" of the CALICE collaboration, on numerous beam tests during the years 2005-2011 [14–16].

Some ASU, similar to the one foreseen for the ILD detector have been operated in two beam test campaigns: first at CERN in 2015, where 3 ASU mounted on test boards behaved as expected [17]; a signal to noise ratio (SNR) - defined as the Most Probable Value of a Landau fit on data, divided by the Gaussian width of the noise – reached typical values of 15-18, with a very limited number of masked channels.

More recently a campaign at DESY using 1-5 GeV electrons, punching through "short slabs", featuring all the elements of the slabs described in section 6.2.1.5 but limited to a

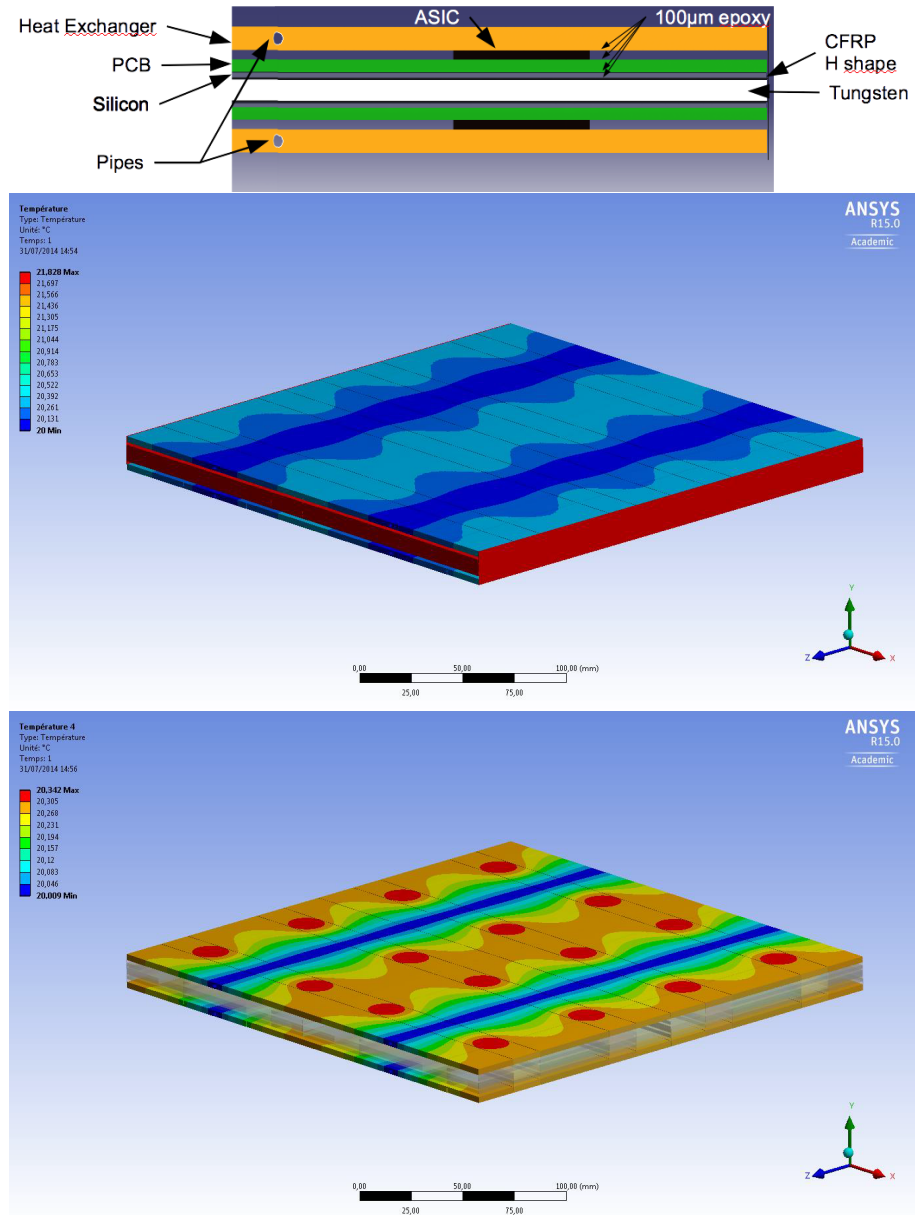


**Figure 6.6:** Top: Transverse section of slab equipped with CO<sub>2</sub> cooling pipes embedded in the cooling plates Left: Heat map over the full module. Right: heat map in the heat exchanger

single ASU on a single side, could reach a SNR of  $\simeq 20$  in average [18].

The collected data is still under analysis for estimated calorimetric performances, but they are expected to be similar to the physics prototype.

The building of a “long slabs” is being actively pursued, and should be completed toward the end of year 2019; the R&D involves all the power, cooling and FE issues for an ILD near the ILC.

The results and design will have to be adapted for a circular collider, where operation *a priori* forbid power-pulsed operations.

## 6.2.2 Scintillator-Tungsten Sandwich Electromagnetic Calorimeter

### 6.2.2.1 Introduction

Alternatively, a sampling calorimeter with scintillator-tungsten structure is proposed. It can be built in a compact and cost effective way. The structure of the ScW ECAL is similar to the SiW ECAL. The major geometry parameters of the ScW ECAL are also studied and optimized, with the similar results of the SiW ECAL. The active layers of the ScW ECAL are consisting of  $5 \times 45\text{mm}^2$  scintillator strips. The scintillator strips in adjacent layers are perpendicular to each other to achieve a  $5 \times 5\text{mm}^2$  effective transverse readout cell size. Each strip is covered by a reflector film to increase collection efficiency and improve uniformity of the scintillation light. Photons from each scintillator strip are read out by a very compact photo-sensor, SiPM, attached at the end of the strip. The SiPM and highly integrated readout electronics make the dead area in the ScW ECAL almost negligible.

Plastic scintillator is a robust material which has been used in many high energy physics experiments. Production of the scintillator strips can be performed at low cost by the extrusion method. Moreover, the number of readout channels can also be significantly reduced due to the strip structure. So the total construction cost of the ScW ECAL is lower than the SiW ECAL. Some key issues which might affect the performance of the ScW ECAL were studied and optimized.

### 6.2.2.2 SiPM dynamic range study

Because each pixel on a SiPM can only detect one photon at once and a few nanoseconds are needed before recovery, the SiPM is not a linear photon detection device, especially in the case of high intensity light input. The application of the SiPM in the CEPC ScW ECAL is a challenge to its dynamic range, which need to be studied.

For a short time light pulse, the response of the SiPM can be theoretically calculated as

$$N_{\text{fired}} = N_{\text{pixel}}(1 - e^{-N_{\text{pe}}/N_{\text{pixel}}}) \quad (6.1)$$

However, for the ScW ECAL, the width of the light pulse should not be ignored, and some pixels of the SiPM can detect more than one photon in an event. The response of the SiPM should be modified as

$$N_{\text{fired}} = N_{\text{eff}}(1 - e^{-N_{\text{pe}}/N_{\text{eff}}}) \quad (6.2)$$

The  $N_{\text{eff}}$  stands for the effective number of pixels on a SiPM, which is relative to the width of the input light pulse. Response curve of 10000 pixel ( $10\mu\text{m}$  pitch size) and 1600 pixel ( $25\mu\text{m}$  pitch size) SiPM with different duration light have been tested. As shown in

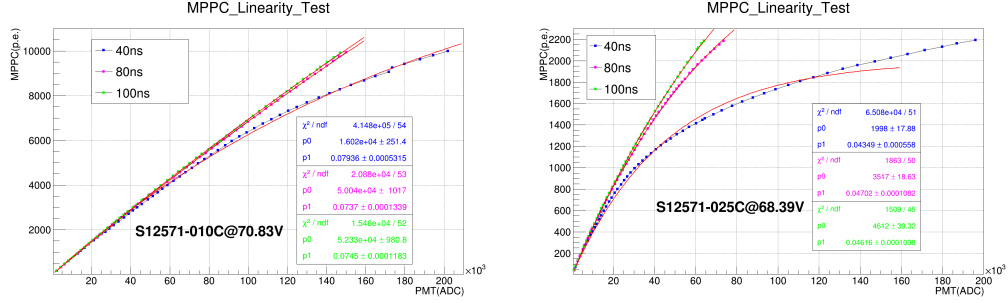


**Figure 6.7:** The response curve of 10000-pixel(left) and 1600-pixel(right) SiPM with different duration light.

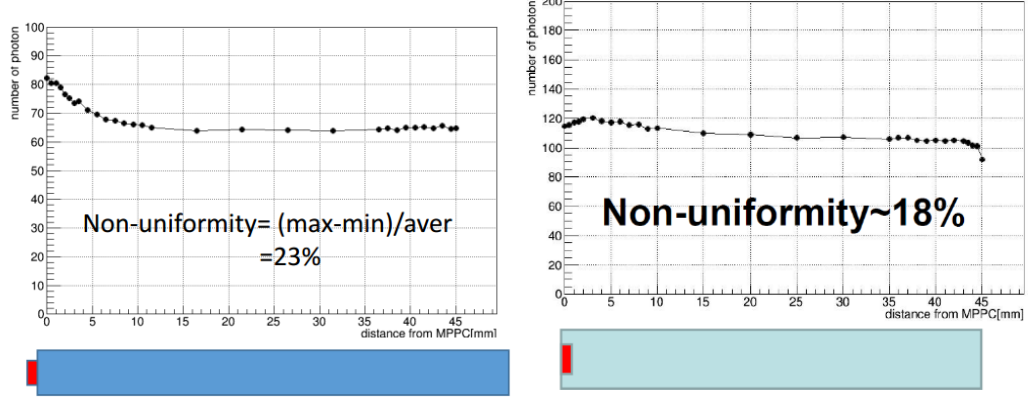


**Figure 6.8:** Scintillator module test results, with the SiPM coupled on the surface (left) or embedded into the strip(right).

Figure 6.7, the output linearity of the device is improved by the increase in the incident light width.

### 6.2.2.3 Scintillator strip test

Because the SiPM is coupled at one end of the scintillator strip, the light output will be non-homogeneous along the length of the scintillator, which will affect the performance of the ScW ECAL. By moving a Sr<sup>90</sup> source along the length of the scintillator, we test the light pulses height read out by the SiPM to study the non-uniformity of the scintillator detector. Figure 6.8(left) is a typical test result of a scintillator module whose light output non-uniformity is 23%. The uniformity can be improved by optimizing the reflection material or the coupling methods of the SiPM to the scintillator strip. Figure 6.8(right) shows a result of a scintillator module with the SiPM embedded into the scintillator strip, and Figure 6.9 is the light output of another scintillator module with different reflector. Scintillators with ESR reflector can give much more light output. We have also test the light output of the scintillator coupled with the SiPM with different pitch size. Two kinds of SiPM have same sensitive area (1mm×1mm), but have pitch size of 25μm and 10μm respectively. The light output of the scintillator with 25μm pitch SiPM is only about 1/3 of the scintillator with 10μm pitch SiPM, shown in Figure 6.10.

### 6.2.2.4 Beam test of a mini prototype

To study the layout, the coupling mode of the scintillator and the SiPM, and further test the minimum ionization particles (MIP). A mini prototype was constructed and tested by test

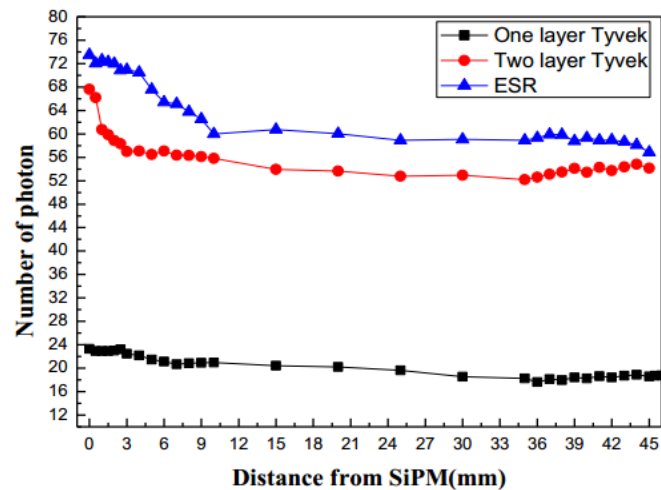


Figure 6.9: light output of scintillator with different reflector.

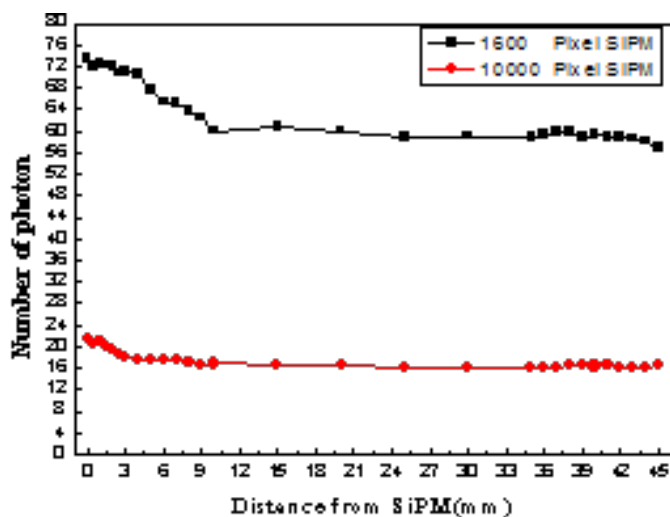
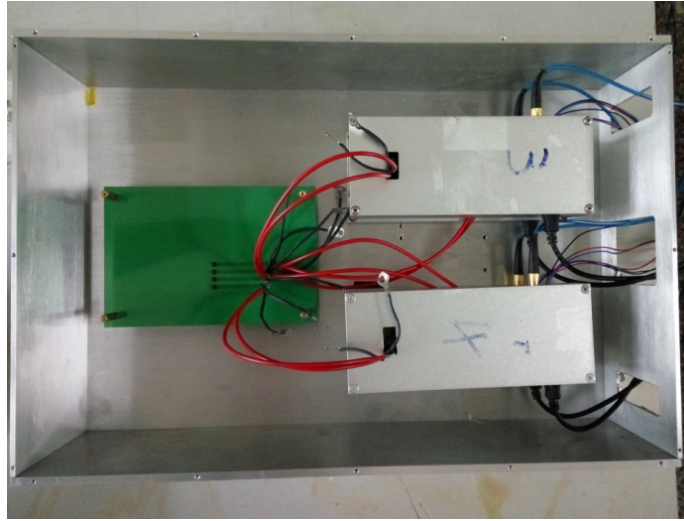


Figure 6.10: light output of the scintillator with different SiPM.



**Figure 6.11:** the picture of the prototype.

beam. The test was carried out at the E3 beam at the IHEP, which could provide proton and pion mixed irradiation. The momentum of the particles was adjusted from 400MeV to 1.1GeV in the test.

The prototype includes four scintillator modules attached tightly to each other, as shown in Figure 6.11. Each module is composed of a BC408 scintillator with a dimension of  $45\text{mm} \times 5\text{mm} \times 2\text{mm}$ , and a Hamamatsu S12571-025P SiPM coupled at the end of the scintillator as a photoelectric conversion device. The prototype is put into an aluminum box for electro-magnetic and light shielding. Figure 6.12 shows the detector layout in the test beam and the schematic of the readout. The beams first pass through two time of flight detectors (TOF) with the distance of 3m for particle identification, and then go through two scintillator counters with the same dimension of total of the four scintillator modules used to estimate the efficiency of the prototype. The prototype is located between the two scintillator counters. The signals from the TOFs and the scintillator counters are directly sent to a wave sampling digitizer (CAEN DT5751). The SiPM from each modules of the prototype is connected to a Hamamatsu driver board (C12332-01), which not only amplifies the signals from the SiPM, but also can eliminate the gain changes of the SiPM caused by the fluctuation of the temperature during the test thanks to its temperature compensation circuit. The signals from the four driver boards are sent to another CAEN DT5751 module to be digitized.

Figure 6.13 are the energy spectrums of pions and protons with momentum of 400MeV/c, 700MeV/c and 1000MeV/c respectively after the system calibration, which indicate the energy deposition in a module. The  $dE/dx$  as a function of the momentum of the particles can be got from the energy spectrums of the module, as shown in Figure 6.14. The values of  $dE/dx$  of protons and pions are consistent with the expected ones with respect to the momentum of the particles. Based on the  $dE/dx$  of pions, we can know the signal of the MIPs from the scintillator module is about 50 photoelectrons.

#### 6.2.2.5 Implementation Example for the Analog Calorimeter Readout

The readout electronics of the ECAL has to provide high dynamic range of energy, while showers of particle may deposit 1~800 MIPs energy in single cell for 100GeV photon.

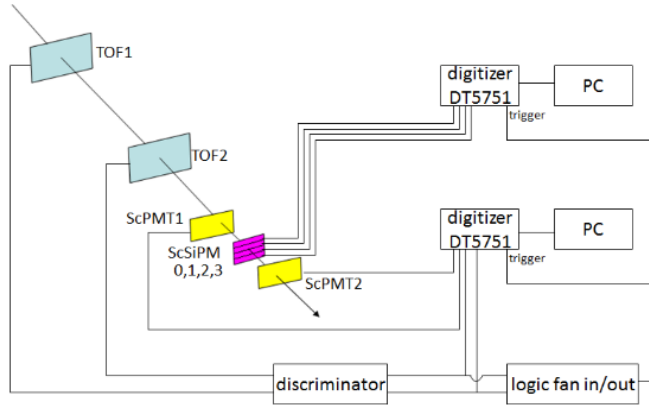


**Figure 6.12:** the schematic of the readout of the prototype.

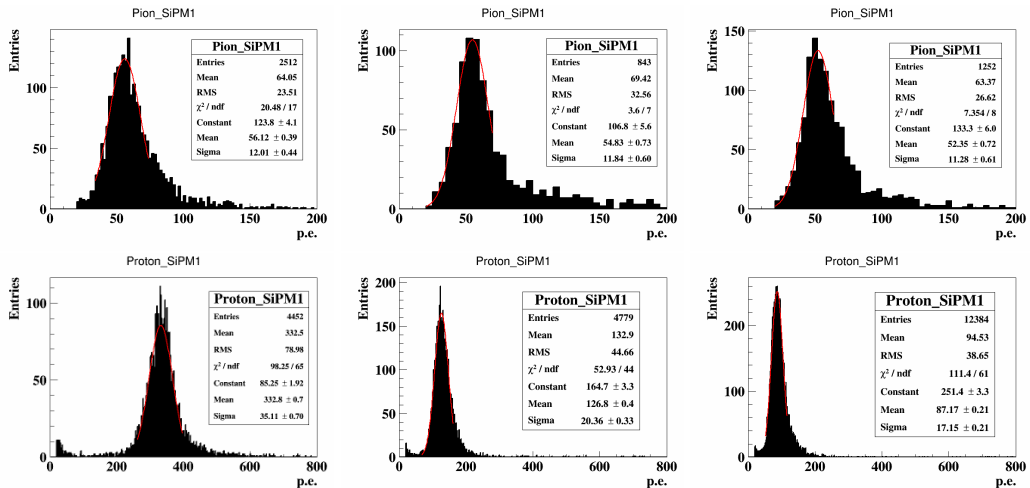


**Figure 6.13:** the energy spectra of pions and protons with momentum of 400MeV/c, 700MeV/c and 1000MeV/c.

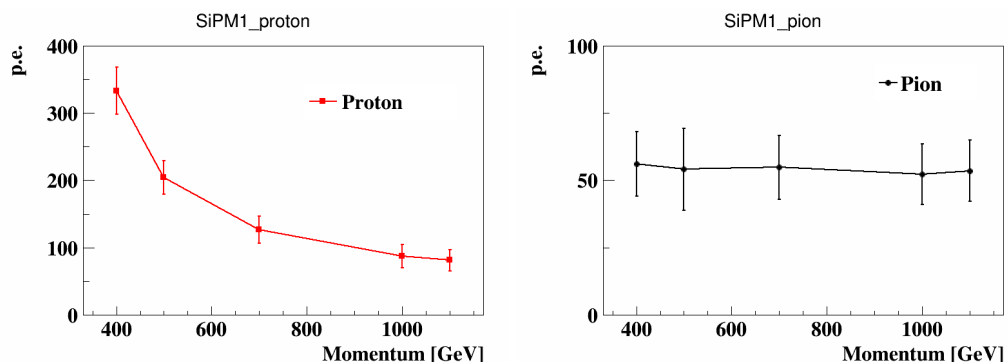


**Figure 6.14:**  $dE/dx$  of protons and pions change with the momentum.

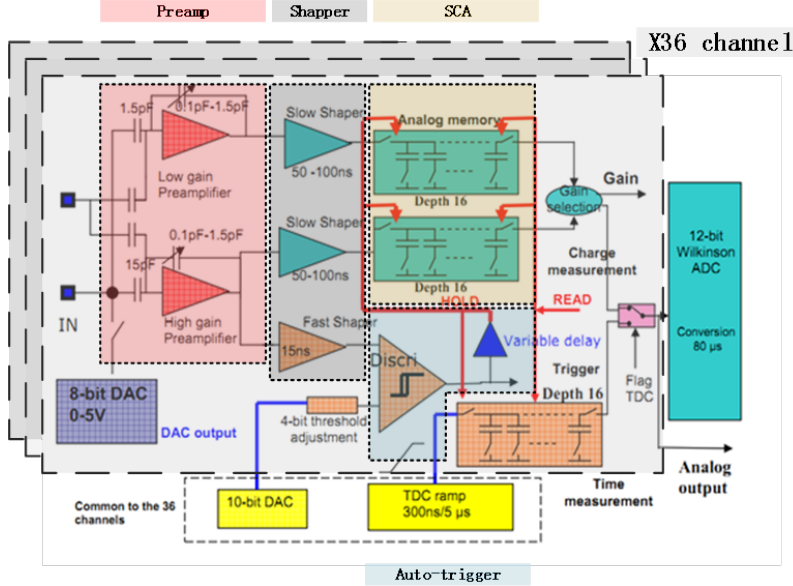


**Figure 6.15:** Schematic view of proposed readout ASIC.

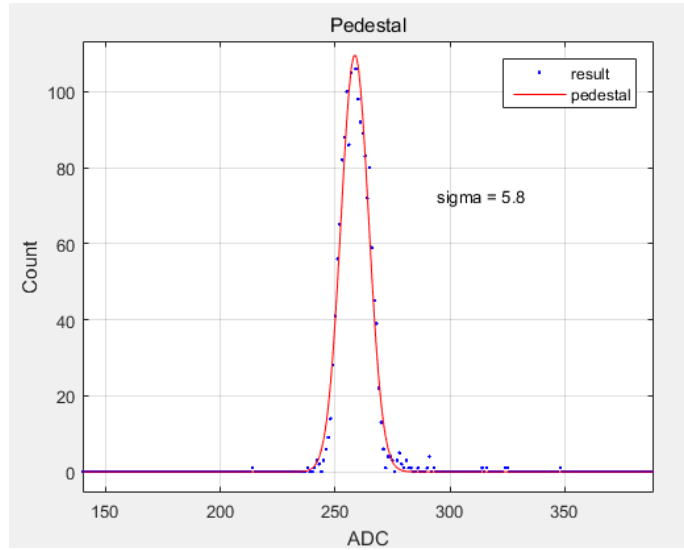
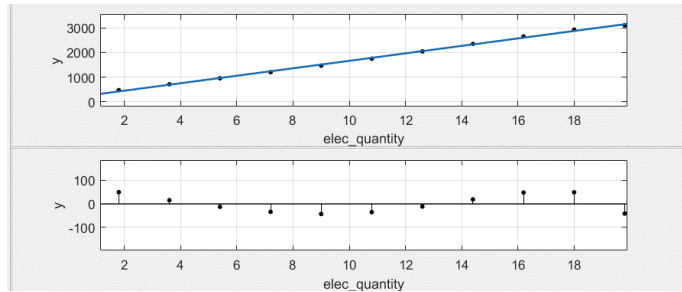
As Particle Flow Algorithm (PFA) is being considered, high granularity requirement need be meet. Granularity of cells in ECAL need be finer than 10mm therefore a large amount of channels need be readout. So multiple-channels-readout-chip is considered.

Electronics consists of two parts: Front-End and Back-End. The Front-End-Electronics (FEE) is embedded into the layers of ECAL. It performs amplification, auto-triggering, digitization and zero-suppression, with local storage of data between the working phases. The Back-End-Electronics play the role of collecting data and configuring chip before system running.

Several studies and existing calorimeter readout electronics have shown that one can obtain optimized energy resolutions using a preamplifier-shaper and digitizing the pulse at peak. For instance, a preamp-shaper-SCA structure of analog circuit applied on ILC HCAL which implemented in ASIC. A similar approach can be applied at CEPC-ECAL. An ASIC named SPIROC2b is considered in present stage. The analog part is schematically depicted in Figure 6.15.

The basic principle consists of a readout chain with an amplifier-shaper using a RC<sub>n</sub>-CR<sub>p</sub> filter delivering a pulse length of about 50-200ns duration for a SiPM pulse signal. This signal is also shaped by a fast shaper in the same time to generate fast and narrow pulse for discriminating. Then the discriminator gives the trigger to Switched-Capacitor-Array (SCA) for locking the peak value of slow-shaped signal. The locked voltage value is corresponding to the charge that circuit received. A 12bits Wilkinson ADC is used for digitizing analog voltage in SCA. Future detailed implementations of the calorimeter front-end electronics for CEPC is still considered using ROC series ASIC but newer version.

The maximum data rate can be estimated as follows. Assuming signal keep coming consistently, SPIROC2b will be continuously switched between three states called Acquisition, AD Converting and Readout. Only in Acquisition state can SPIROC2b receive signal from SiPM and stored in SCA in the rate of about 5MHz. Another two states should be seen as “dead-time” status. There is 16 depth in SCA, so 4us for Acquisition,

**Figure 6.16:** Pedestal noise.**Figure 6.17:** High gain calibration.

according to measurement,  $\sim 4\text{ms}$  for ADC & Readout. So data rate is 16 events per 4ms which equals to 4 kHz. Each fulfilled data packaged is 2 Kbytes in size.

More chip in one layer will multiply the duration of Readout. Assuming that there are 4 chips in one layer. So there is 16ms for Readout. Maximum events rate is reduced to 1kHz and leads to about a transmission of 5Mbyte/s. This can easily be managed with 100M links.

The power consumption in the front-end will be dominated by ASIC and more specifically by analog part of ASIC. Opening all modules, one SPIROC2b is consuming 250.8mW of which about 150mW is consumed by analog part. In actual use, most of cycle is ADC and Readout. It leads to about 150mW power consumption per chip and 4mW per channels.

The electronic calibration and cosmic ray test have been done. From these electronic calibration Figure 6.16 - Figure 6.18, we can see that the noise of readout system is 46fC in RMS and high gain and low gain is 151/pC and 10.3/pC while maximum ADC range is 4096. So dynamic range that from 100fC-300pC of readout system is measured by electronic method. Cosmic ray results shows that the system can distinct MIPs signal from pedestal well and figure out that about 1pC.

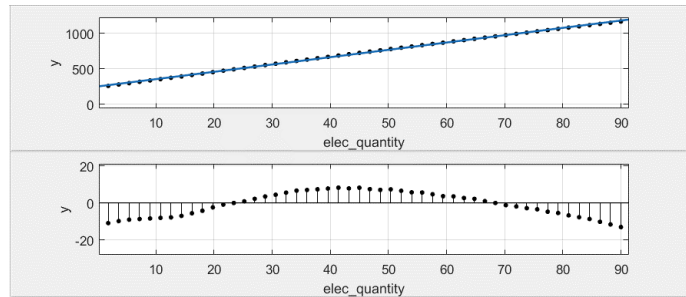


**Figure 6.18:** Low gain calibration.

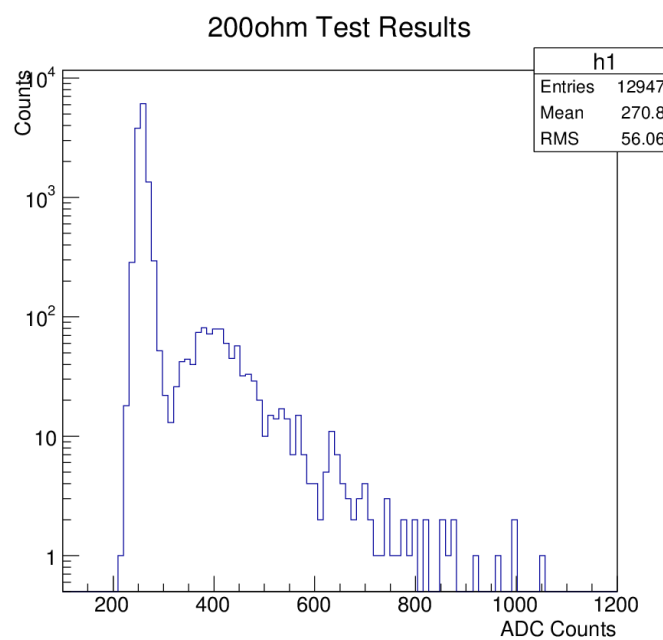


**Figure 6.19:** Cosmic Ray result.

## 6.3 Hadronic Calorimeter for Particle Flow Approach

### 6.3.1 Introduction

High-granularity hadronic calorimeter concept is to play an essential role in PFA-based experiments such as CEPC. It allows to separate the deposits of charged and neutral hadrons and to precisely measure the energy of the neutrals. The contribution of the neutrals to the jet energy, around 10% on average, fluctuates in a wide range from event to event, and the accuracy of the measurement is the dominant contribution to the particle flow resolution for jet energies up to about 100 GeV. For higher energies, the performance is dominated by confusion, and both topological pattern recognition and energy information are important for correct track cluster assignment. High-granularity hadronic calorimeter is thus needed to achieve excellent jet energy resolution.

HCAL are sampling calorimeters with steel as absorber and scintillator tiles or gaseous devices with embedded electronics for the active part. The steel was chosen due to its rigidity which allows to build self-supporting structure without auxiliary supports (dead regions). Moreover, the moderate ratio of hadronic interaction length ( $\lambda_I = 17$  cm) to electromagnetic radiation length ( $X_0 = 1.8$  cm) of iron, allows a fine longitudinal sampling in terms of  $X_0$  with a reasonable number of layers in  $\lambda_I$ , thus keeping the detector volume and readout channel count small. This fine sampling is beneficial both for the measurement of the sizable electromagnetic energy part in hadronic showers as for the topological resolution of shower substructure, needed for particle separation.

The active detector element has very finely segmented readout pads, with  $1 \times 1 \text{ cm}^2$  size, for the entire HCAL volume. Each readout pad is read out individually, so the readout channel density is approximately  $4 \times 10^5/\text{m}^3$ . For the entire HCAL, with  $\sim 100 \text{ m}^3$  total volume, the total number of channels will be  $4 \times 10^7$  which is one of the biggest challenges for the HCAL system. On the other hand, simulation suggests that, for a calorimeter with cell sizes as small as  $1 \times 1 \text{ cm}^2$ , a simple hit counting is already a good energy measurement for hadrons. As a result, the readout of each channel can be greatly simplified and just record 'hit' or 'no hit' according to a single threshold (equivalent to a '1-bit' ADC). A hadron calorimeter with such kind of simplified readout is called a Digital Hadron Calorimeter (DHCAL). In a DHCAL, each readout channel is used to register a 'hit', instead of measure energy deposition, as in traditional HCAL. In this context, gas detectors (such as RPC, GEM) become excellent candidates for the active element of a DHCAL. Another technology option is Analog Hadron Calorimeter (AHCAL) which is based on scintillator with SiPM as active sensor.

A drawing of the HCAL structure is shown in Figure 6.20, the barrel part is made of 5 independent and self-supporting wheels along the beam axis. The segmentation of each wheel in 8 identical modules is directly linked with the segmentation of the ECAL barrel. A module is made of 40 stainless steel absorber plates with independent readout cassettes inserted between the plates. The absorber plates consist of a total of 20 mm stainless steel: 10 mm absorber from the welded structure and 10 mm from the mechanical support of the detector layer. Each wheel is independently supported by two rails on the inner wall of the cryostat of the magnet coil. The cables as well the cooling pipes will be routed outside the HCAL in the space left between the outer side of the barrel HCAL and the inner side of the cryostat.

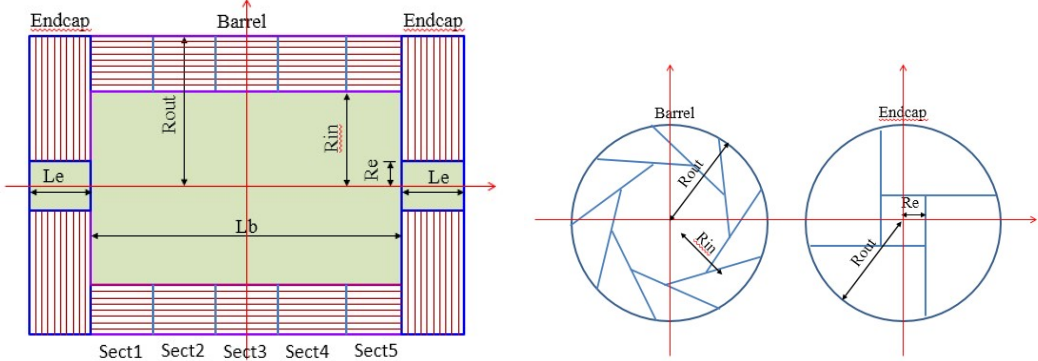


**Figure 6.20:** Longitudinal profile (Left) and transverse section (Right) of the HCAL.

### 6.3.2 Semi-Digital Hadronic Calorimeter (SDHCAL)

#### 6.3.2.1 Introduction

For the CEPC, a SDHCAL based on gaseous detector is proposed. This is motivated by the excellent efficiency and very good homogeneity the gaseous detectors could provide. Another important advantage of gaseous detectors is the possibility to have very fine lateral segmentation. Indeed, in contrast to scintillator tiles, the lateral segmentation of gaseous devices is determined by the readout electronics and not by the detector itself. Active layer thickness is also of importance for what concerns the CEPC hadronic calorimeter to be placed inside the magnetic field. Highly efficient gaseous detectors can indeed be built with a thickness of less than 3 mm. Other detectors could achieve such performance. However, gaseous detectors have the advantage of being cost-effective and discharge free. They are also known for their fast timing performance which could be used to perform 4D construction of the hadronic showers. Such a construction can improve on hadronic showers separation by better associating the energy depots belonging to the same shower from those of other showers. It can also improve on the energy reconstruction by identifying the delayed neutrons and assigning them a different weight.

To obtain excellent resolution of hadronic shower energy measurement a binary readout of the gaseous detector is the simplest and most effective scenario. However, a lateral segmentation of a few millimeters is needed to ensure good linearity and resolution of the reconstructed energy. Such a lateral segmentation leads to a huge number of electronic channels resulting in a complicated readout system design and a too large power consumption.  $1 \times 1 \text{ cm}^2$  cells are found to be a good compromise that still provides a very good resolution at moderate energies. However, simulation studies show that saturation effects are expected to show up at higher energies ( $> 40 \text{ GeV}$ ). This happens when many particles cross one cell in the center of the hadronic shower. To reduce these effects, the choice of multi-threshold electronics (Semi-Digital) readout is chosen to improve on the energy resolution by exploiting the particle density in a more appropriate way. These elements were behind the development of a Semi-Digital Hadronic CALorimeter (SDHCAL) that we propose to equip one of the CEPC future experiments.

Even with a  $1 \times 1 \text{ cm}^2$  lateral granularity of the readout system, a huge number of electronic channels is still needed. This has two important consequences. The first is the power consumption and the resulting increase of temperature which affects the behavior of the active layers. The other consequence is the number of service cables needed to

power, read out these channels. These two aspects can deteriorate the performance of the HCAL and destroy the principle of PFA if they are not addressed properly.

The R&D pursued by the CALICE SDHCAL groups has succeeded to pass almost all the technical hurdles of the PFA-based HCAL. The SDHCAL groups have succeeded to build the first technological prototype [19] of these new-generation calorimeters with 48 active layers of GRPC,  $1\text{m}^2$  each. The prototype validates the concept of high-granularity gaseous detector and permits to study the energy resolution of hadrons one can obtain with such calorimeter.

In order to find out an appropriate option for the active detector of the SDHCAL, two parallel detector schemes, the Glass Resistive Plate Chamber (GRPC) and the Thick Gaseous Electron Multiplier (THGEM) are proposed for the active layers of the SDHCAL.

### 6.3.2.2 GRPC based SDHCAL

**The GRPC scheme** The structure of GRPC proposed as an active layer of the HCAL proposed for CEPC is shown in Figure 6.21. It is made out of two glass plates of 0.7 mm and 1.1 mm thickness. The thinner is used to form the anode while the thicker forms the cathode. Ceramic balls of 1.2 mm diameter are used as spacers between the glass plates. The balls are glued on only one of the glass plates. In addition to those balls, 13 cylindrical fiber-glass buttons of 4 mm diameter are also used. Contrary to the ceramic balls the buttons are glued to both plates ensuring thus a robust structure. Special spacers (ceramic balls) were used to maintain uniform gas gap of 1.2 mm. Their number and distribution were optimized to reduce the noise and dead zones (0.1%).

The distance between the spacers (10 cm) was fixed so that the deviation of the gap distance between the two plates under the glass weight and the electric force does not exceed 45 microns. The choice of these spacers rather than fishing lines was intended to reduce the dead zones (0.1%). It was also aimed at reducing the noise contribution observed along the fishing lines in standard GRPC chambers. The gas volume is closed by a 1.2 mm thick and 3 mm wide glass-fiber frame glued on both glass plates. The glue used for both the frame and the spacers was chosen for its chemical passivity and long term performance. The resistive coating on the glass plates which is used to apply the high voltage and thus to create the electric field in the gas volume was found to play important role in the pad multiplicity associated to a mip [20]. A product based on colloids containing graphite was developed. It is applied on the outer faces of the two electrodes using the silk screen print method, which ensures very uniform surface quality. The measured surface resistivity at various points over a  $1\text{m}^2$  glass coated with the previous paint showed a mean value of  $1.2 \text{ M}\Omega/\square$  and a ratio of the maximum to minimum values of less than 2 ensuring a good homogeneity of the detector.

Another important aspect of this development concerns the gas circulation within the GRPC taking into account that for the CEPC SDHCAL, gas outlets should all be on one side. A genuine system was proposed. It is based on channeling the gas along one side of the chamber and releasing it into the main gas volume at regular intervals. A similar system is used to collect the gas on the opposite side. A finite element model has been established to check the gas distribution. The simulation confirms that the gas speed is reasonably uniform over most of the chamber area. The GRPC and its associated electronics are housed in a special cassette which protects the chamber and ensures that the readout board is in intimate contact with the anode glass. The cassette is a thin box consisting

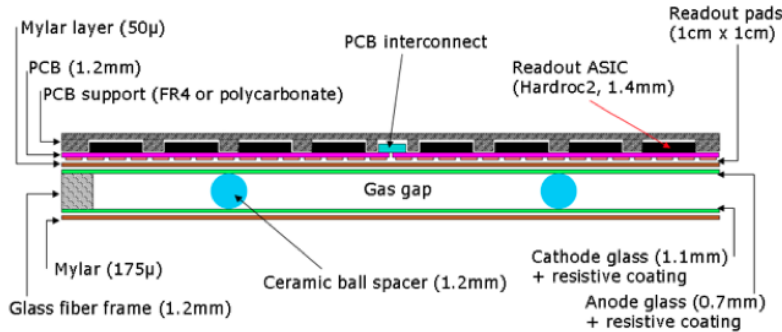


**Figure 6.21:** Cross-section through a  $1\text{ m}^2$  chamber.

of 2.5 mm thick stainless steel plates separated by 6 mm wide stainless steel spacers. Its plates are also a part of the absorber.

The electronics board is assembled thanks to a polycarbonate spacer which is also used to fill the gaps between the readout chips and to improve the overall rigidity of the detector. The electronics board is fixed on the small plate of the cassette. Thanks to tiny screws and the new set is fixed on the other plate which hosts the detector and the spacers. The whole width of the cassette is 11 mm with only 6 of them corresponding to the sensitive medium including the GRPC detector and the readout electronics.

**GRPC technological prototype** An SDHCAL prototype fulfilling the efficiency, robustness and the compactness requirements of the future PFA-based leptonic collider experiments [19] was built. 48 cassettes as the one described above were built. They fulfilled a stringent quality control. It is worth mentioning that 10500 HR ASICs were produced and tested using a dedicated robot for this purpose. The yield was found to be higher than 92%. The ASICs were then fixed on the PCBs to make a  $1\text{m}^2$  and itself fixed on the cassette cover once successfully tested. The cassettes were inserted in a self-supporting mechanical structure that was conceived and built in collaboration with the Spanish group of CIEMAT. The structure is made of Stainless Steel plates of 1.5 cm each. The plates were machined to have an excellent flatness and well controlled thickness. The flatness of the plates was measured using a laser-based interferometer system. It was found that the flatness of the plates are less than 500 microns. This results guarantees that for the SDHCAL V structure proposed for ILD, a tolerance of less than 1mm is achievable. The prototype construction lasted less than 6 months. A commissioning test at CERN in 2011 allowed to understand the whole system behavior. In April 2012 the prototype was exposed to pion, muon, electron beams of both the PS and the SPS of CERN Figure (6.22). Power-pulsed mode was applied to the whole prototype using the beam cycle structure (0.3 ms time duration for the PS beam and 9 s for the SPS beam every 45s). The data were collected continuously in a triggerless mode. Figure 6.23 shows the efficiency (left) and pad multiplicity (right) of the prototype's GRPC chambers measured using the muon beam. Figure 6.24 shows a display of two events collected in the SDHCAL. One is produced by a pion interaction (left) and the other by an electron interaction (right).

The SDHCAL prototype results obtained with a minimum data treatment (no grain correction) show clearly that excellent linearity and good resolution [21] could be achieved on large energy scale as can be shown in Figure 6.25 where results obtained in two different beam lines are obtained using the same detector configurations. Useless to mention that

the high granularity of the SDHCAL allows one to study thoroughly the hadronic showers topology and to improve on the energy resolution by, among others, separating the electromagnetic and the hadronic contribution. The separation between close-by showers will also get big benefit thanks to the high granularity on the one hand and to the very clean detector response ( $< 1 \text{ Hz/cm}^2$ ) on the other hand. The results obtained with the SDHCAL [22] confirm the excellent efficiency of such separation thanks to the SDHCAL performance. In addition, the high-granularity of the SDHCAL allows to extract the track segments of hadronic showers in a very efficient way [23]. The track segments (Figure 6.26) are then used to study the detector behavior in-situ. This is a simple but powerful control and calibration tool for a running calorimeter.

The quality of data obtained during several campaigns of data taking at the CERN PS and SPS beam lines validates completely the SDHCAL concept. This is especially encouraging since no gain correction was applied to the electronics channels to equalize their response. Still, improvement was further achieved by applying gain and threshold correction schemes in terms of the calorimeter response homogeneity.

A digitizer describing the response of the G<sub>R</sub>PC within the SDHCAL was developed [24]. It allows to study the SDHCAL behavior in a realistic manner in the future experiments.

In parallel to the prototype construction, a single cassette was tested in a magnetic field of 3 Tesla (H2 line at CERN) applying the power-pulsed mode. The TB results [25] indicated clearly that the use of the power-pulsed mode in such a magnetic field is possible. The behavior of the detector (efficiency, multiplicity..) was found to be similar to those obtained in the absence of both the magnetic field and the power-pulsed mode.

**Readout electronics** To read out the SDHCAL an ASIC called HARDROC2 was developed. To solve the problem of connections related to the high number of electronic channels, the option of a detector embedded electronics using the DAISY chain scheme was chosen and Printed Circuit Board (PCB) were conceived for the readout of large detectors G<sub>R</sub>PC.

- **Front-end ASIC:** The HARDROC2 chip (HR) implements a multi-threshold readout which integrates the functionalities of amplification, shaping, digitization, internal triggering and local storage of the data. Each of its 64 channels consists of a fast low impedance current preamplifier with 8-bit variable gain (in the [0, 2] range) followed by 3 fast shapers (15 ns shaping time). A low offset discriminator is present on each path and the three corresponding thresholds establish the multi-level readout. The thresholds are set using three integrated 10-bit Digital to Analog Converters (DAC). The outputs of the three discriminators are then encoded and stored in an internal digital memory latched by a trigger event. A trigger is generated when one of the lowest level discriminators is fired but can also be configured on the other thresholds. A frame consists of the 64 encoded discriminator outputs, plus a 24-bit time-stamp and a chip identifier is stored after a trigger is received. Noisy channels could be easily masked via the configuration parameters control. In order to avoid fake triggers produced by noisy channels, the output of each discriminator can be switched off from the trigger generator logic via the configuration parameters control (Slow Control hereafter) commands. The response of all the channels can be calibrated by injecting an analog signal through an integrated  $2 \pm 0.02 \text{ pF}$  input test capacitor; this is a useful tool to make the response of the different channels as uniform as

possible [20]. The ASIC contains a 127-frame long digital memory. This allows to work in a triggerless mode and keep all the data accumulated during the bench crossing.

Once the memory is full the acquisition is stopped, the readout is performed and the ASIC can start acquisition again. The Gray-coded time-stamp is derived from an external 5 MHz clock. An essential feature of the HR is the possibility to be operated in the power-pulsing mode (PP) that consists of switching off almost all power-consumption functionalities in between the bench crossings (BC) of the electron beams. In the case of CEPC this mode may allow a moderate reduction of the power consumption but this is not enough to prevent the detector heating due to the power consumption. Therefore an embedded active cooling system is needed.

- **Active Sensor Units:** To read out the 1 m<sup>2</sup> detector of the SDHCAL prototype, an electronic board with the same size is needed. This electronic board is an important piece in the present design. It hosts both the pick-up pads and the ASICs in addition to the connections between the pads and the ASICs and those linking the different ASICs. To ensure good transmission qualities and low cross-talk, 50 cm × 33 cm, 8-layer Printed Circuit Board (PCB) is designed. Each of these ASUs hosts 24 chips to read out 48×32 pads of 1cm<sup>2</sup> each. This dressed PCB is dubbed Active Sensor Unit (ASU). The routing of each input signal from its own pad up to chip pin has been carefully optimized to reduce the cross-talk. The rooting was conceived so two of the ASUs can be associated to form one slab hosting 48 ASICs. Each slab is then connected to one Detector InterFace board (DIF). The connection between the DIF and the slab as well as the connection of the two ASUs is performed thanks to tiny connectors allowing the different clocks, signals as well as the power to circulate between the two ASUs. Three slabs are then assembled to form the required electronics board. To ensure the same electric reference level for the six ASUs, the GND layer of the six ASUs is connected thanks to a copper gasket on all the common sides. Similar schemes could be proposed for GRPC detectors with larger size.

- **Front-end and back-end boards:** The interface between the ASUs and the data acquisition system (DAQ) is realised by the DIF. The main elements of the DIF is an FPGA and USB, HDMI and SAMTEC connectors. It manages the control signals (*e.g.* clock, busy/ready, external/internal trigger, power-pulsing) and supply power to the ASICs and also performs the readout of the ASIC memories. DIFs are read out by other FPGA-based boards called Data Concentrator Cards (DCC). They can be connected up to 9 DIFs through HDMI links and are controlled by a synchronous DCC (or SDCC). The SDCC can connects to up to 9 DCCs to which it distributes the clock and the commands. It is also connected to the computer network for the user to control the DAQ.

- **Data Acquisition software:** To exploit the data collected by the SDHCAL detectors an acquisition software was developed. This software is organized in three parts. The first one allows to access the hardware devices (DIF, SDCC) through an FTDI chip associated to each of these devices. It transmits the configurations parameters to ASICs through these devices and collect the data as well. The second part is the configuration data base. It gives the possibility to store and retrieve all parameters needed by the DAQ system. The database itself is hosted on an Oracle server. To interface this SQL database with the DAQ software and to allow users to insert and query data without knowledge of SQL, a C++ library has been written. A special care was taken to allow to download the parameters associated to a given parameters of the prototype (roughly 550000 parameters) in few seconds. The third part concerns the data collection. Data from different DIFs may be readout at a different times but will have the same Bench Crossing IDentifier (BCID)

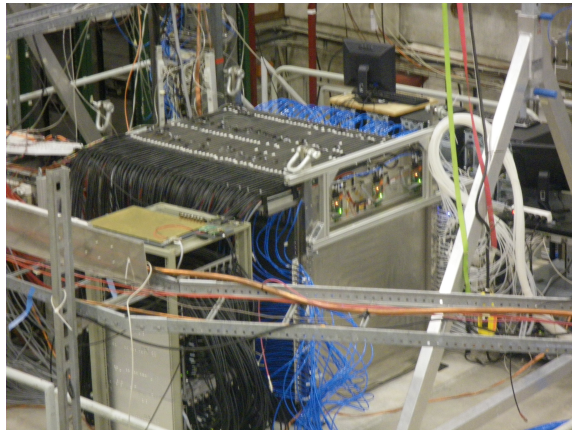


**Figure 6.22:** The SDHCAL prototype in beam test at CERN.

for a given trigger. The logical way to keep synchronicity is to store in a BCID indexed map the buffers of all read DIFs but it requires to manage memory allocation, access and cleaning. This was achieved thanks to the abilities offered by recent Linux kernels to use file based shared memory. In addition, whenever several computers are involved in the data taking, as it is the case for the SDHCAL prototype, a communication framework is needed. The CMS data acquisition XDAQ framework was chosen. This provides communication tools, an XML description of the computer and software architecture, a web-server implementation of all data acquisition application and a scalable event builder. A monitoring system was also developed to have an online follow-up of the acquisition during data collection.

**Preparation for future experiments** A genuine self-supporting mechanical structure to host the hadronic calorimeter of future PFA-based leptonic collider experiments was fully studied. The structure (called V-structure) was conceived to eliminate the projective holes and cracks so none of the particles produced close to the detector centre could escape detection. The V-structure has additional advantages. It eliminates in principle the space between the barrel and the Endcaps avoiding the shower deformation which results not only because of this space but also of the different cables and services needed in CMS-like mechanical structures. In this structure the different services such as the gas tubes, data collection and electric cables of both the barrel and the Endcaps are taken out from the outer radius side. Detailed studies have shown that the deformation of this structure is extremely low and its robustness was verified experimentally with the SDHCAL technological prototype built with a self-supporting structure respecting the spirit of the V one. Services and Integration issues were also worked out. Besides, realistic costing was performed , based on the prototype experience.

**current SDHCAL R&D** Large GRPC of  $1\text{m}^2$  were developed and built for the technological prototype. However, larger GRPC are needed in the SDHCAL proposed for future leptonic collider experiments. These large chambers with gas inlet and outlet on one side need a dedicated study to guarantee a uniform gas gap everywhere notwithstanding the angle of the plate. It is necessary also to ensure an efficient gas distribution as it was done for the  $1\text{m}^2$  chambers. To obtain this different gas distribution systems were studied. A new scheme with two gas inlets and one outlet was found to ensure an excellent homo-

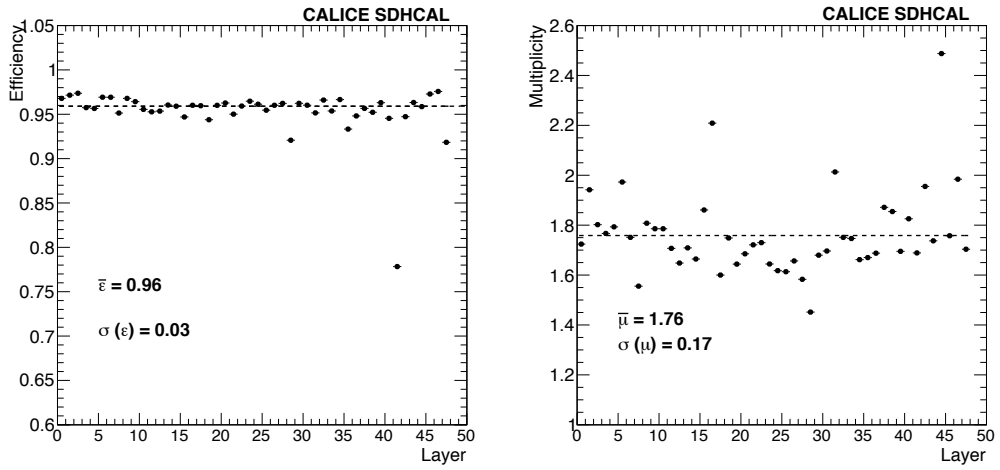


**Figure 6.23:** Left: Efficiency of the GRLC detectors of the SDHCAL. Right: the pad multiplicity of the GRLCs. One third of the chamber 42 was not instrumented.

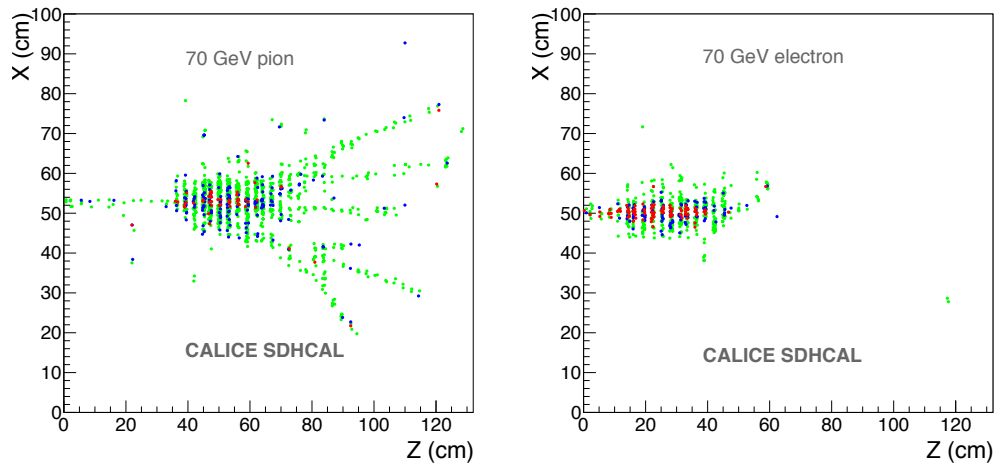


**Figure 6.24:** Left: event display of an 70 GeV pion interaction in the SDHCAL prototype. Right: Event display of a 70 GeV electron interaction in the SDHCAL prototype.

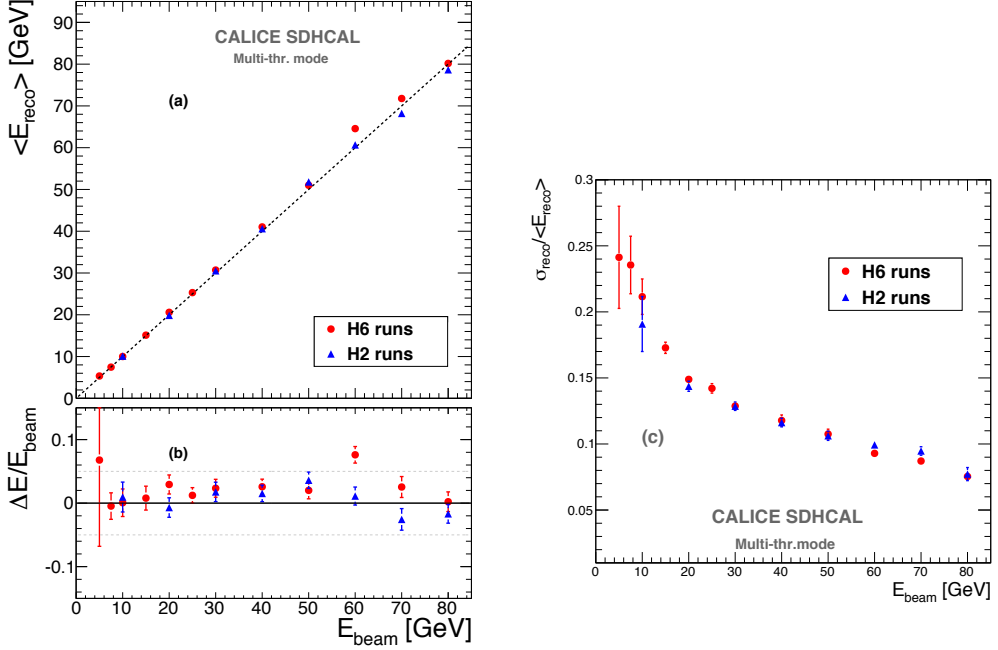


**Figure 6.25:** Left: a) Reconstructed energy of the hadronic showers collected in both H2 and H6 SPS beamlines. b) the relative deviation of the reconstructed energy with respect to the beam energy. Right: Relative energy resolution of the reconstructed hadronic shower. Pion beam of H6 beamline is largely contaminated by protons at high energy ( $>50$  GeV).

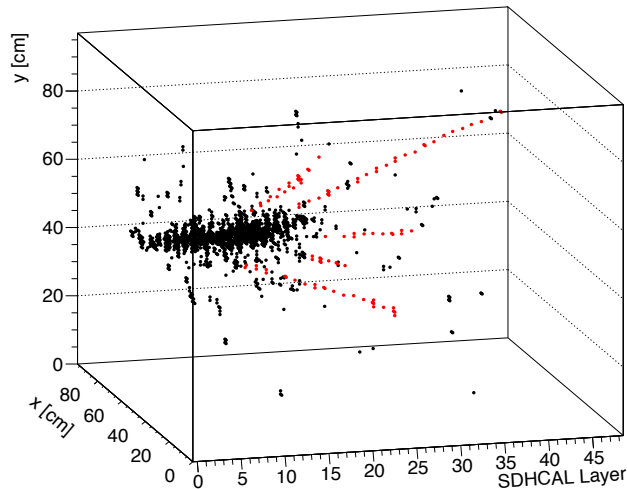


**Figure 6.26:** A 3D event display of a pion interaction event showing the track segments extracted by applying a hough transform technique.

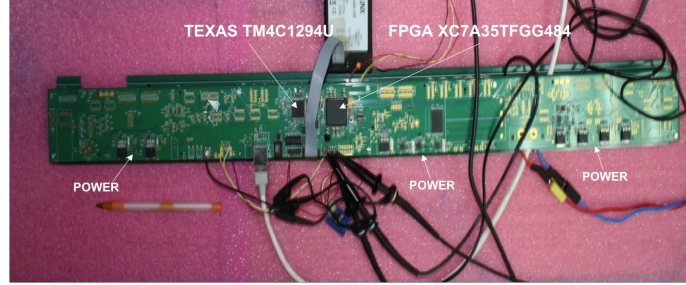


**Figure 6.27:** A new Detector InterFace (DIF) allowing to address up to 432 ASICs of 64 electronic channels each.

geneity of the gas distribution. This system will be used in the near future to build large detectors exceeding  $2\text{m}^2$ . The readout of such chambers needs also to be as efficient as the one of the technological prototype  $1\text{m}^2$ . An upgrade of the HR ASIC allowing larger dynamic range (01-50 pC) was conceived, produced and successfully tested. The new ASIC (HR3) allows to be directly addressed and easily bypassed in case of failure thanks to the I2C protocol. In addition and contrary to the HR2, the 64 channels of the new ASIC are independent which allows a better calibration procedure. Furthermore, a new interface board (DIF) is conceived to control the ASICs synchronization and data transfer. Indeed, the space left between the active layer of one module and the cryostat maybe very short in future leptonic experiments ( $< 5\text{ cm}$ ). This means that the DIF components should be optimized to cope with the volume availability. A new design with new functionalities of the DIF is proposed. A TPC/IP protocol is adopted for data transfer and a TTC one for the clock synchronisation. A microprocessor implemented on the new DIF is in charge of the communication between the ASICs and the DIF's FPGA. The new DIF shown in Fig. 6.27 is capable to address up to 432 ASIC. A new PCB design that allows to assemble few boards to cover up to  $3\text{ m}^2$  GRPC detector was also conceived. Care is taken to ensure robust and flexible but still tiny connection between the different PCB to build a large one. Fig. 6.28 shows a picture of such a PCB equipped with the HR3 ASICs. Finally a new technique based on electron beam welding is being tested to build a mechanical structure. This intends to reduce the steel quantity used to assemble the absorber plates while guaranteeing a minimum deformation. First attempts have taken place at CERN recently 6.29 and more study is ongoing to determine the best protocol one should follow to obtain optimal results. Finally, to cope with the heating produced by the embedded readout system in case of limited or even the absence of use of the Power Pulsing system, a new active cooling system is being studied. Figure 6.30 shows a study of a water-based cooling system to absorb the excess of heat in the SDHCAL. The cooling system is very simple but very effective as well. It allows to keep the average temperature as well as the temperature dispersion of the GRPC well under control.

### 6.3.2.3 THGEM-based DHCAL

**The THGEM scheme** The THGEM can be built in large quantities at low cost, which might make them suitable for the large CEPC HCAL. THGEM detectors can provide flexible configurations, which allow small anode pads for high granularity. They are robust and fast, with only a few nano-seconds rise time, and have a short recovery time which allows a higher rate capability compared to other detectors. They are operated at a relatively low voltage across the amplification layer with stable high gain. The ionisation



**Figure 6.28:** A new PCB equipped with he HR3 ASICs. The PCB is 100 cm × 33.3 cm. Several PCBs could be connected thanks to tiny flexible connectors to read out very large GReP detectors.

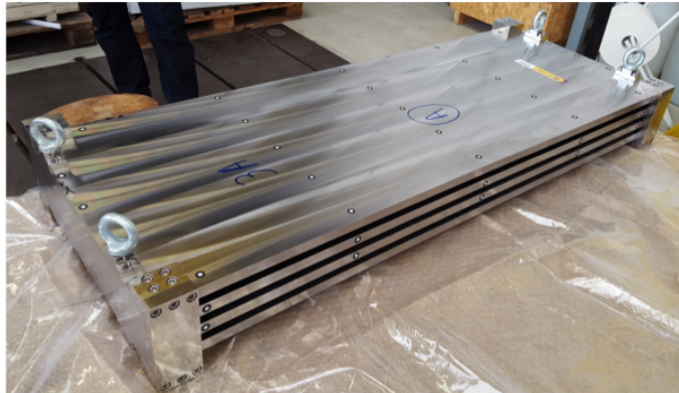


**Figure 6.29:** A prototype of an SDHCAL mechanical structure assembled using the electron beam welding technique.

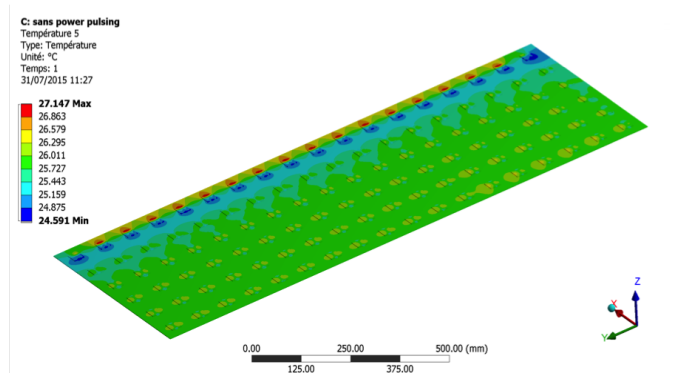


**Figure 6.30:** Temperature distribution in an active layer of the SDHCAL operated with no power pulsing. The cooling system is made of a circulating water inside copper tubes in contact with the ASICs.

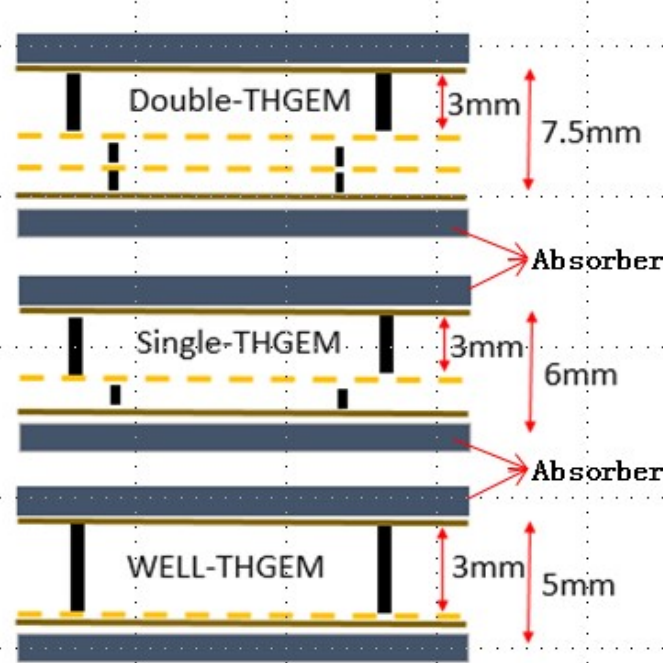


**Figure 6.31:** Structure of THGEM based detector for DHCAL.

signal from charged tracks passing through the drift section of the active layer is amplified using a single layer or WELL-type THGEM structure. The amplified charge is collected at the anode layer with pads at zero volts. As the HCAL is located within the coil, WELL-THGEM, a single layer structure with thinner thickness, as shown in Fig. 6.31, can be considered as the sensitive medium, to keep the HCAL compact.

Digital readout has been proposed to limit the total amount of data, which simplifies the data treatment without comprising the energy resolution performance. The readout electronics of the DHCAL will be integrated into the sensitive layer of the system, thus minimising dead areas. Large electronics boards are assembled together to form extralarge boards before being attached to the THGEM. The board assembly will utilise a mechanical structure made of 4 mm stainless steel plate. In addition, to keep the HCAL as compact as possible, the fully equipped electronic boards are designed to be less than 2 mm thick in total.

A THGEM based detector for DHCAL has been designed with 40 layers in total. Each layer contains 2.0 cm thick stainless steel, 0.8 cm thick THGEM and readout electronics with  $1 \times 1 \text{ cm}^2$  readout pads. As THGEM production technology matures, the maximum area of THGEM is limited only by the size of the CNC drilling area. Its low price, robustness against occasional discharges, high gain and count rate capability of up to  $10\text{MHz}/\text{cm}^2$  make THGEM very attractive for building the DHCAL. THGEM is cheaper and more robust than GEM, and has a higher counting rate capability than GPC. As illustrated in Fig. 6.31, the total thickness of the sensitive medium is 5 mm, which consists of 3 mm drift gap, 1 mm transfer gap and 1 mm induction gap. The absorber between the active layers is made of 20 mm thick stainless steel. The thickness of the readout electronics board is about 3 mm, and the total thickness of a single sensitive layer is less than 10 mm. Each layer corresponds to about 1.2 radiation length and 0.65 nuclear interaction

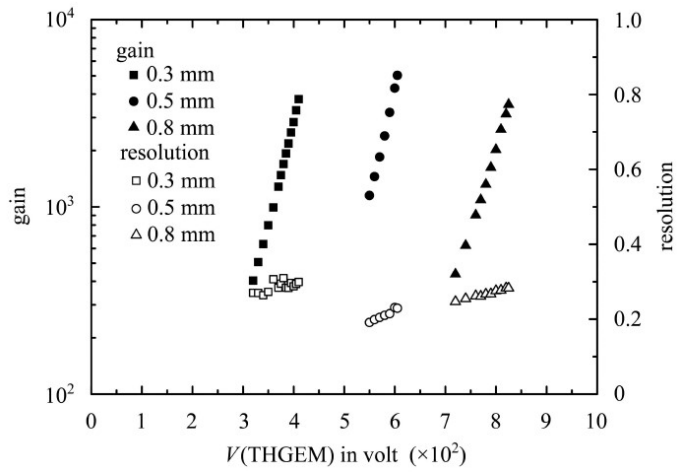


**Figure 6.32:** Gain and energy resolution of THGEM detector obtained with  $^{55}\text{Fe}$ .



**Figure 6.33:** The maximum size of THGEM produced in domestic currently ( $40 \times 40 \text{ cm}^2$ ).

length. The whole DHCAL detector is evenly divided into 40 layers, with a total stainless steel absorber thickness of 4.7 nuclear interaction lengths.

**THGEM prototype** A THGEM with an area of  $40 \times 40 \text{ cm}^2$  has been successfully fabricated, as shown in Fig. 6.33, and a gain of  $2 \times 10^5$  has been achieved with a double THGEM, with an energy resolution of about 20%. The THGEM produced has the following features: 1) standard PCB processes are used, which keeps the cost low; 2) excellent performance in terms of energy resolution, gas gain and stability (as shown in Fig. 6.32); 3) Rim around the hole formed by full-etching process, the size of which can be varied between  $10 \mu\text{m}$  and  $90 \mu\text{m}$ , as depicted in Fig. 6.32 - this allows adjustment according to gas requirements.

Fig. 6.34 shows the schematic diagram of a new THGEM detector, where a micro-plate directly attached to the readout plate, since the micro-porous structure similar to a well, known as the well-type THGEM (WELL-THGEM). This structure contains of a single-layer THGEM, so that the thickness of detector can be reduced to  $4 \sim 5 \text{ mm}$ , and the total thickness of the detector including ASIC electronics could be lowered to about 6 mm.

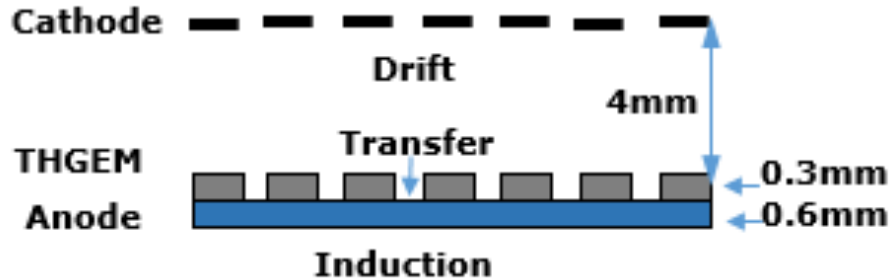


**Figure 6.34:** The schematic diagram of the WELL-THGEM.

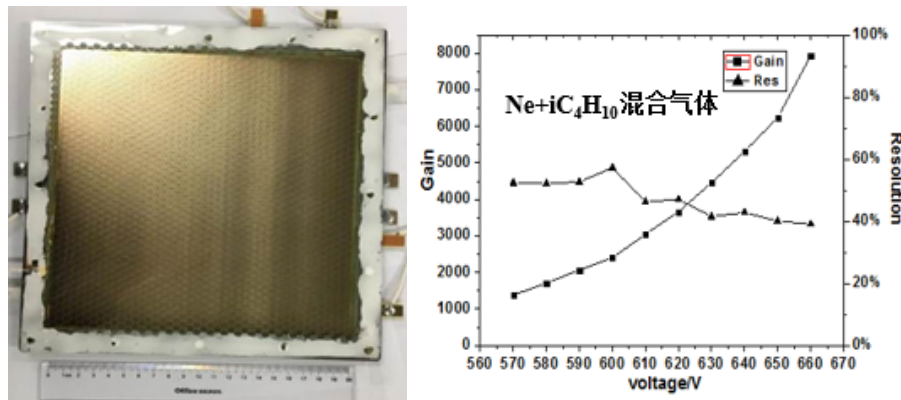


**Figure 6.35:** The photograph(left) and performance (right) of the WELL-THGEM detector.

A  $20\text{cm} \times 20\text{cm}$  WELL-THGEM detector using thin-type THGEM have been developed, and the basic performances such as the gain curve, uniformity and energy resolution were studied and shown in Fig. 6.35.

In addition, Researches on large THGEM detectors have been carried out. Single THGEM detectors and Well-THGEM detectors are being developed to reduce detector instability and inefficiency. Gas recycling systems are built to lower gas consumption and pollution. The achieved THGEM detection rate of  $1\text{ MHz}/\text{cm}^2$  with efficiency greater than 95% already meets the CEPC requirements.

**THGEM digital readout system** A MICRO-mesh gaseous structure Read-Out Chip (MICROROC), which is developed at IN2P3 by OMEGA/LAL and LAPP microelectronics groups was used to read out the THGEM-based SDHCAL. The MICROROC is a 64-channel mixed-signal integrated circuit based on 350 nm SiGe technology. Each channel of the MICROROC chip contains a very low noise fixed gain charge preamplifier which is optimized to cover a dynamic range from 1 fC to 500 fC and allow a input detector capacitance of up to 80 pF, two gain-adjustable shapers, three comparators for triple-threshold readout and a random access memory used as a digital buffer. Otherwise, it have a 10-bit DAC, a configuration register, a bandgap voltage reference, a LVDS receiver shared by 64 channels etc. A 1.4 mm total thickness is achieved by using the Thin Quad-Flat Packaging (TQFP) technology.

The readout system structure as shown in Fig. 6.36 is developed on the Scalable Readout System (SRS), which is proposed by the RD51 Collaboration. It is composed of a front-end board (FEB), a detector interface board (DIF) and a data acquisition card (DAQ).

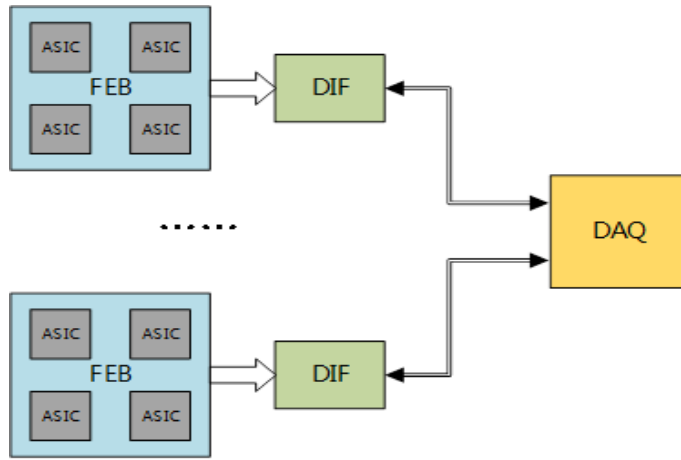


**Figure 6.36:** The schematic diagram of the readout system.

The FEB (also called ASU-Active Sensor Unit) carries all the front-end ASIC, together with the readout plane of GEM detector. The DIF in charge of ASIC control and data connection, plugs to the FEB using high density connector. The DAQ card is designed to serve several DIF boards. It distributes the clock, command and trigger to different DIF and gather the data from DIF boards.

The FEB is the combination of readout pads of GEM detector and readout ASICs. In order to minimize the dead-area of the detector, the FEB is designed to use blind and buried via technology. Considering the signal integrity and costs, 8 ~ 10-layer PCB is a suitable choice. The thickness of this kind of PCB can be as thin as 1.2 mm. This means contain the 1.4 mm MICROROC, the total thickness of FEB can be made within 3 mm. Limited by PCB manufacturing technology, a well-performance FEB can be made as large as  $50\text{cm} \times 50\text{cm}$ . If a  $1\text{m}^2$  prototype is made, it necessary to combine 4 FEB into one detector layer.

The DIF controls the FEB and gather the data of ASIC and can be tailored to the particular front-end ASIC with the particular application, giving the users the freedom of choice for the front-end circuit. Just changing the ASIC and DIF, the same design can be used both in ECAL and HCAL. Considering the data rate and costs, the master device of DIF can be some low-cost FPGA and the communication interface to the DAQ can be both USB type C or fiber-optical.

The DAQ card accesses the command from a server and controls several DIF. The design goal of the DAQ card is a universal controller for both ECAL and HCAL. Once a mature DAQ card is finished, it can be in common use even if we change the front-end ASIC.

Besides the readout ASIC and card, the clock synchronization design is an important block of the system. There are two kinds of clock source in the readout system, local clock and global clock (Usually, this kind of clock may be hundreds or thousands of meters from calorimeters). The local clock goes through the PLL and low-skew fan-out chip to the DIF, then the DIF distribute the clock to the FEB for local synchronization. If a global clock source is used, it is necessary to module there clock to optical signal and distribute the clock through fiber-optical. Another circuit call Clock and Data Recover (CDR) is needed for clock rebuild. The rebuild clock is global synchronized and can be used as local clock in one DAQ card.

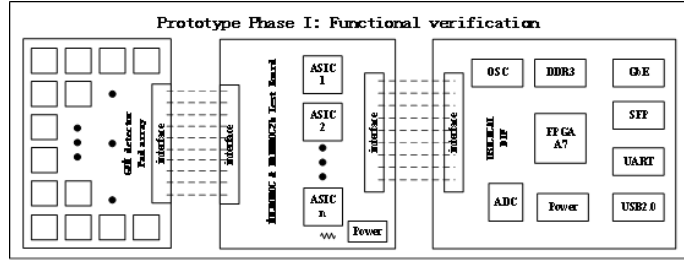


**Figure 6.37:** The diagram of the phase I design.



**Figure 6.38:** Pictures for the phase I design.

A phase I design (in Fig. 6.37 and Fig. 6.38) is completed to verify this kinds of readout structure and to test the performance of the MICROROC chip. In this design we separate the front-end ASIC from the detector readout plane for single test the ASIC. It contains the readout array of the GEM detector, front-end ASIC board and DIF board. The structure of the design is shown in figure 2. The GEM detector is  $30\text{cm} \times 30\text{cm}$ , and the readout pad detector is  $1\text{ cm}^2$ . To ensure signal integrity and low cross talk the readout plane is designed 8-layer PCB with 4 ground plane to separate the signal and shield. The pads signal is connector to the front-end ASIC board via soft-board made from kapton. The front-end ASIC board composed by 4 ASIC controlled in daisy chain. The DIF board controls the front-end ASIC board and transmit data to the upper monitor. The main controller of DIF is Xilinx A7 100T series, a low cost FPGA. The data can be readout via USB2.0 or fiber-optical or Giga-bit Ethernet. We also reserve an ADC on DIF for monitoring the analog test signal. Figure 3 shows the picture of these three board. The primary performance studies for this design have been carried out. For all the ASIC channel, the maximum noise is 0.35 fC, which means it beyonds the best performance of this ASIC distinguishing at least 2fC signal. The linear region of the high gain shaper reaches to  $\sim 140$  fC, and the low gain shaper is  $\sim 500$  fC. All the result shows that this ASIC can work well with the detector and the readout scheme is effective.

In order to optimize the design, a next stage design (shown in Figure 6.39) based on the test results have been proposed and put into effort. In this version, the MICROROC chips are planed to be mounted on the bottom side of the readout plane, utilizing blind buried via technology. A 10-layer PCB with 3 ground plane and 2 power plane will ensure good signal integrity and low crosstalk. Considering the cost and performance, we choose 2 kinds of blind via (Layer1 - Layer2 and Layer9 - Layer10) and 1 kinds of buried via (Layer2 - Layer9). This board is the real FEB in the system structure. The design diagram is shown in figure 4. Besides FEB, the design of the DIF board is going on the same time. The DIF can plug to FEB directly or through a soft-board made from kapton. After the DIF design, we will consider the design of DAQ board. We can share the same DAQ board with ECal readout system. The DIF is connected to DAQ through USB type C wire

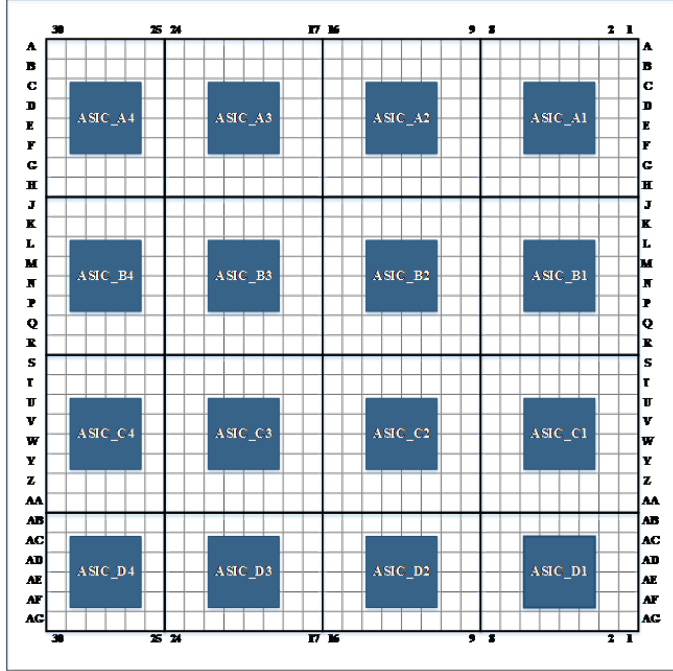


**Figure 6.39:** The Design scheme for next stage FEB.

or fiber-optical. Besides the SRS readout structure, a new system name FELIX is under research, which can make the whole system trigger less readout.

### 6.3.3 Analog Hadronic Calorimeter based on Scintillator and SiPM

A high-granularity hadronic calorimeter plays an essential role in PFA-based experiments such as CEPC. It allows separation of the energy deposits from charged and neutral hadrons. The contribution of the neutrals to the jet energy, around 10% on average, fluctuates over a wide range from event to event. The HCAL is a sampling calorimeter with steel as the absorber and scintillator tiles with embedded electronics. The moderate ratio of hadronic interaction length ( $I=17\text{cm}$ ) to electromagnetic radiation length ( $X_0 = 1.8 \text{ cm}$ ) of steel, allows a fine longitudinal sampling in terms of  $X_0$  with a reasonable number of layers.

Various calorimetry options are being developed to address challenges from the stringent performance requirements on future lepton collider experiments for precision measurements of the Higgs boson and for searches of physics beyond Standard Model. Within the CALICE collaboration, a large technological prototype using scintillator tiles and SiPMs is currently being built to demonstrate the scalability to construct a final detector via automated mass assembly. Though this prototype is aimed for the future International Linear Collider (ILC), the outcome of CALICE-AHCAL R&D activities can be an essential input for the conceptual design of the hadron calorimeter system at the future Circular Electron Positron Collider (CEPC).

#### 6.3.3.1 AHCAL geometry and simulation

The AHCAL consists of 40 sensitive and absorber layers, and the thickness is about 100cm. The AHCAL barrel consists of 32 super modules, each super module consists of 40 layers, fig-

ure 6.40 shows the AHCAL structure. Figure 6.41 shows the AHCAL one layer structure. The scintillator tiles wrapped by reflective foil are used as sensitive medium, interleaved with stainless steel absorber. The thickness of active layer is 4 mm to 5 mm, it depend the thickness of scintillator thickness.

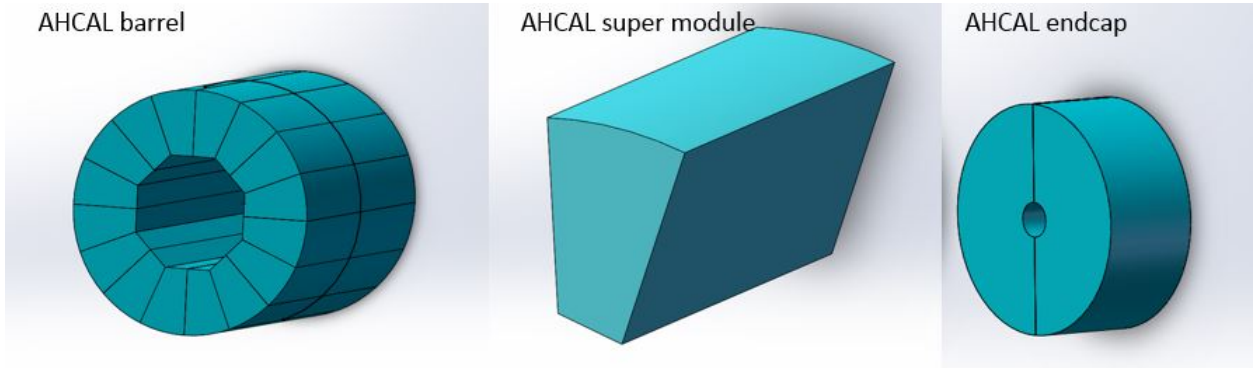


**Figure 6.40:** Side view of one layer in AHCAL

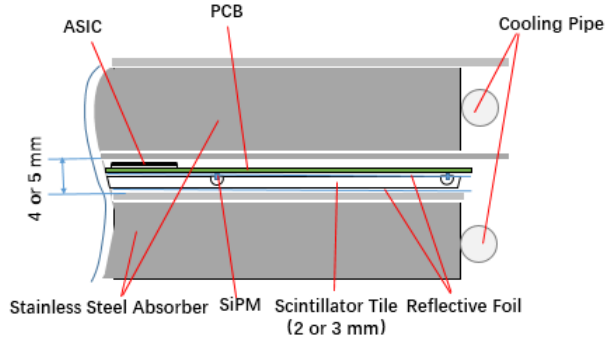


**Figure 6.41:** Side view of one layer in AHCAL

The structure of scintillator tiles is shown in Figure 6.42. A dome-shaped cavity was processed in the center of the bottom surface of each tile via mechanical drilling and polishing. The diameter and height of cavity are 6mm, 1.5mm, respectively, as shown in Figure 6.42 (right). This design of cavity can improve response uniformity and decrease the dead area of HCAL.

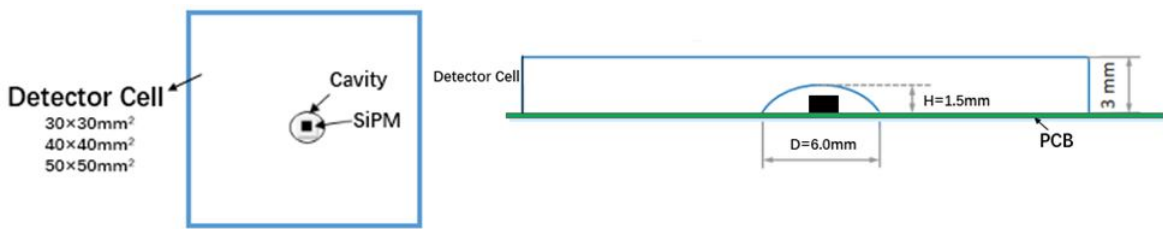


**Figure 6.42:** Top view of a detector cell (left) and sectional view of a detector cell with a dome-shaped cavity (right)

The AHCAL prototype detector simulated by Geant4 which was encapsulated in toolkit including several models. The detector model used here was CEPC\_v1 detector model and the sub detector was SiCal. The geometry information was extract by Mokka at

runtime and the generated events was stored in Slcio, which contains primary information regarding the energy deposition, hit position, time and Monte Carlo particle causing the energy deposition. It can read out by Marlin and translate into Root files for analyzing. The ECAL was simulated 30 layers. The HCAL is a structure of 40 active layers interleaved with 20 mm steel absorber plates. Each active layer is assembled from 3mm plastic scintillator, also the readout layer thickness is 2mm PCB, detector cell size is  $30 \times 30 \times 3$  mm<sup>3</sup>. And the TCMT, we simulate 20 layers and each layer is the same component and material as HCAL. Their structure is shown in Figure 6.43.

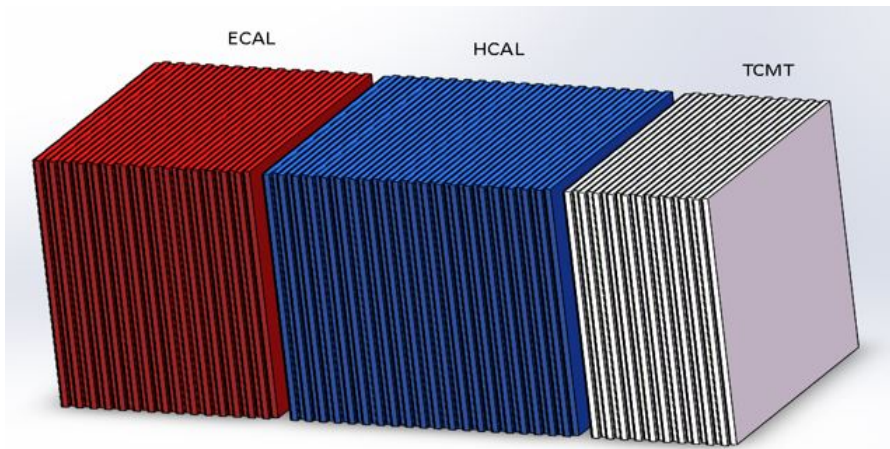


**Figure 6.43:** The structure of simulated calorimeters which is a part of the simplify geometry. Red part is the ECAL, Blue part is the HCAL, and white part is the TCMT

$$E_{REC} = a \times E_{ECAL} + b \times E_{HCAL} \quad (6.3)$$

For getting the resolution of calorimeters (ECAL and AHCAL) which structure was show in figure 6.43. Formula 6.3 is the energy reconstruction formula, the coefficients a and b in this formula represent ECAL and HCAL calibration constant. After optimization, the calibration constants are a=44.4 and b=44.2 respectively which were corrected by energy of 60GeV. Calibration constants can correct the energy leakage from the calorimeters. So it can be used formula 6.4 for calculating the resolution. The energy resolution result shows in figure 6.44. For the resolution is better than the result of CALICE, the reason should be simulation ignore the response difference between detector cells. For the energy linearity, the slope value is 0.99, which means the reconstruction energy is essentially linear.

$$\frac{\sigma}{E} = \frac{p_0}{\sqrt{E}} + p_1 \quad (6.4)$$

### 6.3.3.2 Plastic Scintillator cell measurement

The basic tile size was optimized with respect to particle separation capability and found to be  $30 \times 30$ mm<sup>2</sup>. The simulation results suggest that it is possible to use the detector cells of larger sizes. For example, it will reduce nearly two-thirds electronics channels by using  $50 \times 50$ mm<sup>2</sup> size detector cell instead of  $30 \times 30$ mm<sup>2</sup> size. Therefore, the construction

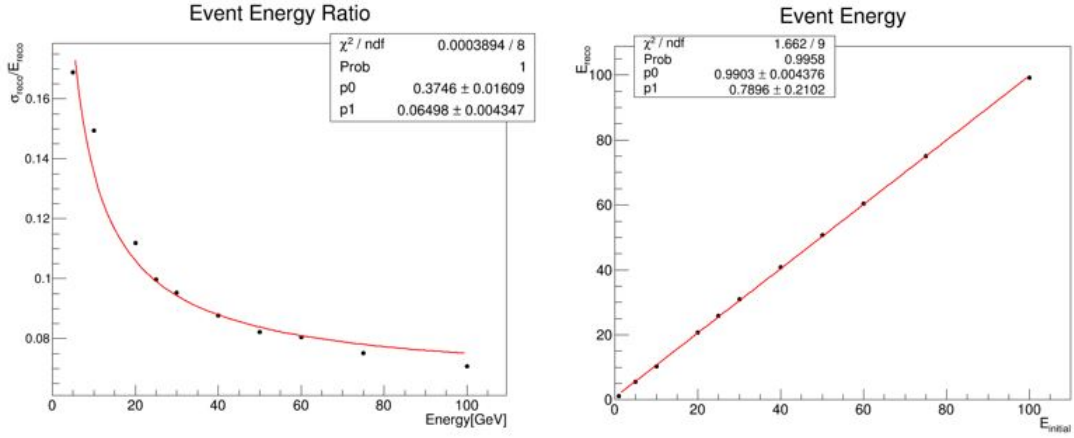


**Figure 6.44:** Left figure is energy resolution, right figure is the result of reconstruction energy linearity

costs can be greatly reduced if the larger detector cells can meet the physics requirements. Two larger sizes of detector cells were considered. Four kinds of scintillator (BC408) tiles with different sizes were fabricated and tested, and they are  $30 \times 30 \times 3\text{mm}^3$ ,  $40 \times 40 \times 3\text{mm}^3$ ,  $50 \times 50 \times 3\text{mm}^3$  and  $30 \times 30 \times 2\text{mm}^3$ .

The SiPM is soldered onto a readout Printed Circuit Board (PCB) and the scintillator tile wrapped by ESR reflective foil is directly glued onto the PCB. Such a cavity design provides enough space for the SiPM package and improves collection efficiency of the light produced by incident particles penetrating the tile at different positions. The SiPM is readout by the Hamamatsu electronic readout board (C12332-01) which has the function of temperature compensation. The time instability of signal amplitude (ADC channel) of SiPM is from 17.59% to 2.38% in the range of 22°C to 30°C owing to temperature compensation from the board, as shown in Figure 6.45.

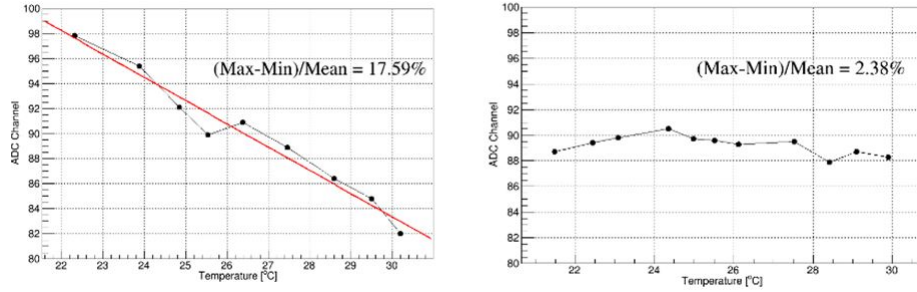


**Figure 6.45:** SiPM signal amplitude varies with temperature, before (left) and after (right) temperature compensation electronics (Hamamatsu C12332-01)

**Uniformity measurement:** A strongly non-uniform tile response can lead to a distortion of the energy reconstruction in a complete calorimeter, and also compromises the calibration of the detector cells based on single particle signals [4]. The response uniformity of a SiPM inside the cavity of a scintillator tile has been measured with a 90Sr source, as shown in Figure 6.46. The trigger scintillator ( $5 \times 5 \times 3\text{mm}^3$ ) and 90Sr source were fixed. A detector cell, which was mounted on a step motor, can be finely moved between 90Sr source and the trigger scintillator. Uniformity scans were accomplished by

horizontally translating the detector cell in a step size of  $5 \times 5 \text{ mm}^2$ . The electronics data acquisition system is shown in Figure 6.47.

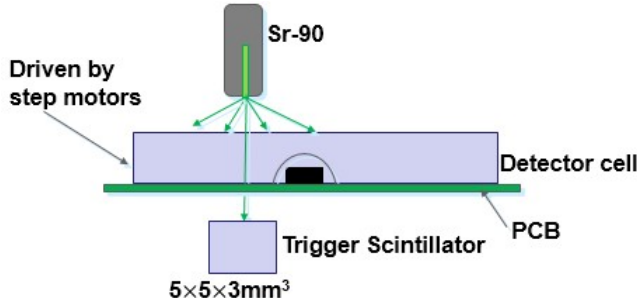


Figure 6.46: Setup of uniformity measurement

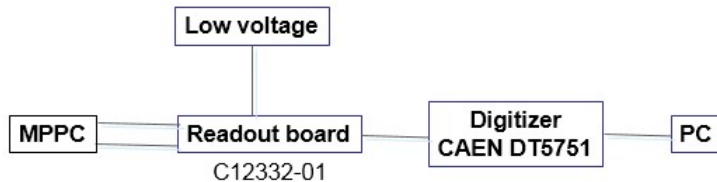
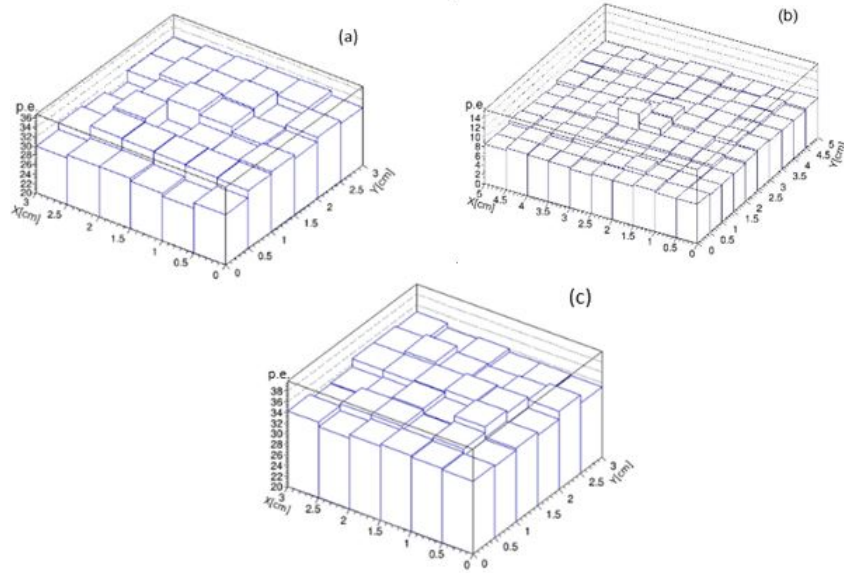


Figure 6.47: Block diagram of data acquisition

Three different sizes tiles ( $30 \times 30 \times 3 \text{ mm}^3$ ,  $30 \times 30 \times 2 \text{ mm}^3$  and  $50 \times 50 \times 3 \text{ mm}^3$ ) were tested by the Hamamatsu MPPC S12571-025P and S13360-025PE. The photosensitive area of module MPPC S12571-025P is  $1 \times 1 \text{ mm}^2$  containing 1600 pixels, and each pixel is  $25 \mu\text{m} \times 25 \mu\text{m}$  in size. The MPPC S13360-1325PE whose sensitive area is  $1.3 \text{ mm} \times 1.3 \text{ mm}$  contains 2668 pixels. The spatial distribution of p.e. (photon equivalents) number with different detector cell areas are shown in Figure 6.48. So the p.e. number presents signal amplitude of different tile areas. It can be seen that the number of p.e. in the center area is a little higher than that of the surrounding area because the MPPC is placed in the center area and there is less self-absorption in the area close to the MPPC. The global mean response is around 32.2 p.e. and 100% of the cell area is within 10% deviation from the mean value for  $30 \times 30 \times 3 \text{ mm}^3$  cell. The global mean response is around 34.29 p.e. and 100% of the cell area is within 10% deviation from the mean value for  $30 \times 30 \times 2 \text{ mm}^3$  cell. The three detector cells show good response uniformity. The global mean response is around 8.57 p.e. and 94% of the cell area is within 10% deviation from the mean value for  $50 \times 50 \times 3 \text{ mm}^3$  cell.

**Cosmic-ray measurement:** The cosmic-ray test setup for measuring responses of scintillator cells to muons is shown in Figure 6.49. The detector cell is placed between two trigger scintillators ( $20 \times 20 \times 3 \text{ mm}^3$ ) tiles. A lead is placed between the detector cell and bottom trigger scintillator to select higher energy cosmic ray events. The coincidence of two trigger signals ensures a muon track passing through the detector cell. Four kinds of tiles with different sizes ( $30 \times 30 \times 3 \text{ mm}^3$ ,  $40 \times 40 \times 3 \text{ mm}^3$ ,  $50 \times 50 \times 3 \text{ mm}^3$  and  $30 \times 30 \times 2 \text{ mm}^3$ ) were measured.

The single photon spectrum of SiPM was used to calibrate the test system, as shown in Figure 6.50 (left). The cosmic-ray MIP response spectrum is shown in Figure 6.50 (right). It is fitted by a Landau convoluted with Gaussian distribution.



**Figure 6.48:** The uniformity measurement result of  $30 \times 30 \times 3 \text{ mm}^3$ (a),  $50 \times 50 \times 3 \text{ mm}^3$ (b)and  $30 \times 30 \times 2 \text{ mm}^3$ (c)detector cell

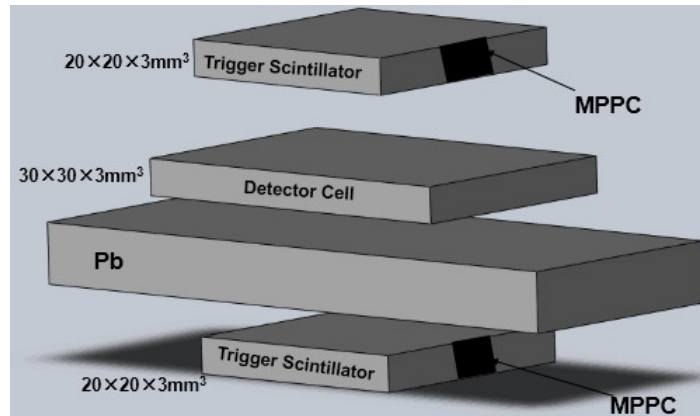


**Figure 6.49:** Schematic diagram of cosmic-ray measurement setup

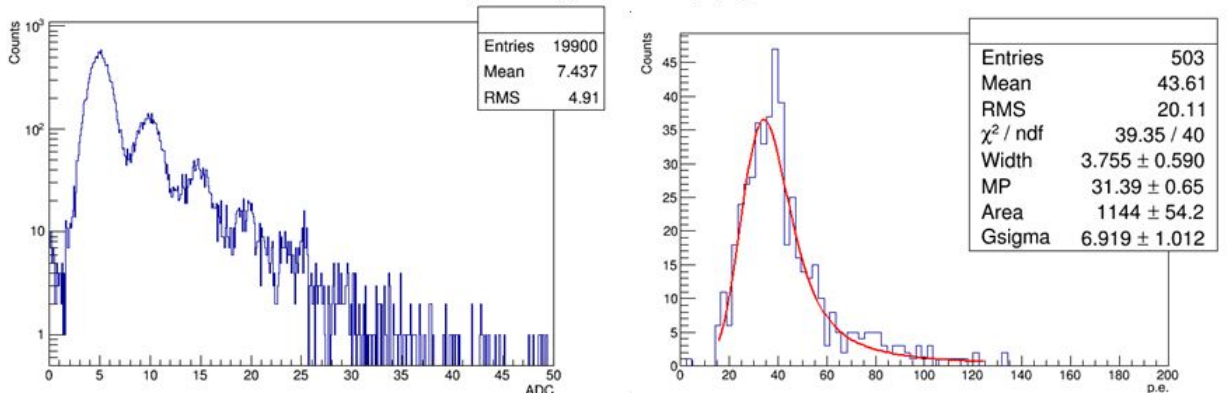


**Figure 6.50:** Single photon spectrum of MPPC (left) and responses to muons of  $30 \times 30 \times 3 \text{ mm}^3$  detector cell (right)

Seven detector cells of different sizes, polishing methods and wrapping foil types were measured and summarized in figure 6.51. The larger the area of the cell is, the less p.e. are detected, and the results of same size cells varied greatly because of the polishing methods. As is shown in the table that the ESR foil performs better than the TYVEK reflective foil. The cell with the size of  $30 \times 30 \times 2\text{mm}^3$  detected  $33.89 \pm 0.49$  p.e. because of the larger photosensitive area of MPPC.

No. <sup>o</sup>	Detector Cell <sup>o</sup>	MPPC Type <sup>o</sup>	Reflective Foil Type <sup>o</sup>	Mean N <sub>p.e.</sub> <sup>o</sup>	Polishing Methods <sup>o</sup>
1 <sup>o</sup>	$30 \times 30 \times 3\text{mm}^3$ <sup>o</sup>	S12571-025P <sup>o</sup>	ESR <sup>o</sup>	$31.39 \pm 0.65$ <sup>o</sup>	Ultra Precise Polishing <sup>o</sup>
2 <sup>o</sup>	$30 \times 30 \times 3\text{mm}^3$ <sup>o</sup>	S12571-025P <sup>o</sup>	ESR <sup>o</sup>	$22.55 \pm 0.7$ <sup>o</sup>	Precise Polishing <sup>o</sup>
3 <sup>o</sup>	$30 \times 30 \times 3\text{mm}^3$ <sup>o</sup>	S12571-025P <sup>o</sup>	ESR <sup>o</sup>	$18.92 \pm 0.39$ <sup>o</sup>	Rough Polishing <sup>o</sup>
4 <sup>o</sup>	$30 \times 30 \times 3\text{mm}^3$ <sup>o</sup>	S12571-025P <sup>o</sup>	TYVEK <sup>o</sup>	$13.63 \pm 0.33$ <sup>o</sup>	Precise Polishing <sup>o</sup>
5 <sup>o</sup>	$40 \times 40 \times 3\text{mm}^3$ <sup>o</sup>	S12571-025P <sup>o</sup>	ESR <sup>o</sup>	$14.89 \pm 0.73$ <sup>o</sup>	Precise Polishing <sup>o</sup>
6 <sup>o</sup>	$50 \times 50 \times 3\text{mm}^3$ <sup>o</sup>	S12571-025P <sup>o</sup>	ESR <sup>o</sup>	$9.87 \pm 0.43$ <sup>o</sup>	Precise Polishing <sup>o</sup>
7 <sup>o</sup>	$30 \times 30 \times 2\text{mm}^3$ <sup>o</sup>	S13360-1325PE <sup>o</sup>	ESR <sup>o</sup>	$33.89 \pm 0.49$ <sup>o</sup>	Precise Polishing <sup>o</sup>

**Figure 6.51:** Cosmic-ray measurement results of detector cells with different sizes

**MIPs Detection efficiency:** The detection efficiency of  $30 \times 30 \times 3\text{mm}^3$  and  $50 \times 50 \times 3\text{mm}^3$  were measured by the cosmic ray test. The detection efficiency of  $30 \times 30 \times 3\text{mm}^3$  and  $50 \times 50 \times 3\text{mm}^3$  cells are 99%, 98.2%, respectively. According the cosmic-ray test result, the detection efficiency of  $30 \times 30 \times 2\text{mm}^3$  with S13360-025PE MPPC also can reach to 98

Several size plastic scintillator detector cells of AHCAL were tested. The response uniformity, cosmic-ray responses and detection efficiency of detector cells were measured. The good response uniformity and high detection efficiency results show that both  $30 \times 30 \times 3\text{mm}^3$  and  $50 \times 50 \times 3\text{mm}^3$  cells are acceptable for AHCAL. The size of detector cell will be decided by the simulation result.

### 6.3.3.3 NDL EQR-SiPM for CEPC AHCAL

SiPM with epitaxial quenching resistors (EQR SiPM) is one of the main SiPM technologies now under development [16,17]. This kind SiPM was developed in China. As shown in Figure 6.52, each APD cell (pixel) forms a high electric field, composing an enriched region between N-type epitaxial silicon substrate and P++ cap layer, and it employs the un-depleted region in the epitaxial silicon layer below P/N junction as the quenching resistor. Compared to conventional SiPM configurations that employ poly-silicon quenching resistors on the device surface, it is easier to achieve high density and small micro APD cells, thus obtaining a small junction capacitor; it is also easy to realize low resistance for the quenching resistors, simply based on the resistivity of the epitaxial layer and the geometrical scale. As a result, a low RC time constant of the pixel, or a short recovery time and fast counting rate for the EQR SiPM, can be expected. In addition, thanks to the high geometrical fill factor of the EQR SiPM with a high density of micro APD cells, both wide dynamic range and adequate PDE can be realized at the same time, which satisfactorily resolves the conflict between dynamic range and PDE existing in most commercial SiPMs with poly-silicon stripes as quenching resistors.

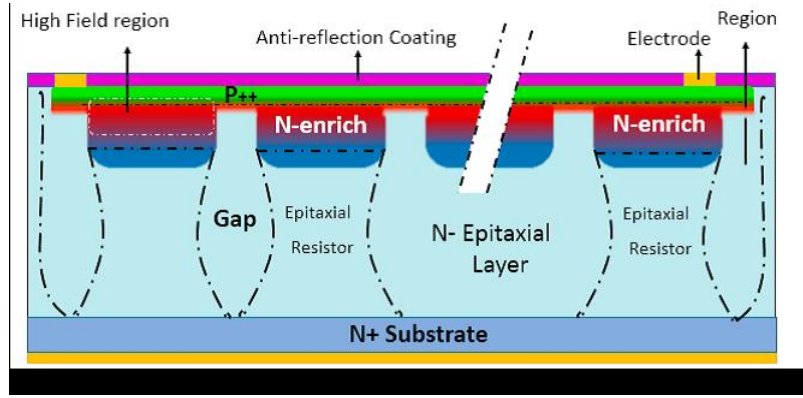


**Figure 6.52:** Schematic structure of EQR SiPM; APD cell consists of N-enriched regions forming high electric fields between the N-type epitaxial silicon wafer and the P++ surface layer, the un-depleted region in the epitaxial silicon layer below the P/N junction as the quenching resistor, and the APD cells are isolated from each other by the Gap depletion region.

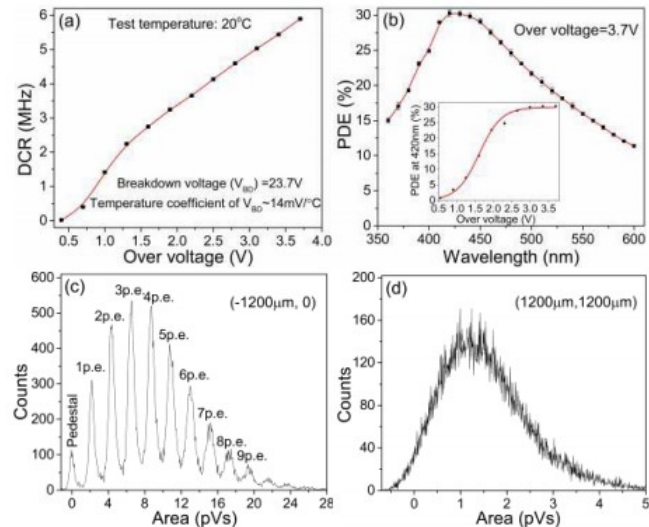


**Figure 6.53:** Characteristics of NDL EQR PS-SiPM. (a) DCR vs over voltages. (b) PDE vs the wavelength of 360nm-600nm at over voltage of 3.7V; peak PDE is at 420nm and is improved with the increase of over voltage as shown in the inset. (c), (d) show the pulse area distribution collected by cathode at the incident light positions of (1200um, 0) and (1200um, 1200um) respectively. Because of the pedestal electronic noise, the pulse area is starting at negative values.

Furthermore, the fabrication technology of NDL EQR-SiPM is simple, it omits the fabrication steps for producing quenching resistors on the surface; thus, the price of NDL EQR-SiPM is low. Its good property and low price can meet AHCAL requirement, and it will be tried to be used on CEPC-AHCAL detector. Figure 6.53 show some performance of NDL EQR-SiPM, and figure 6.54 show the performance compare between NDL EQR-SiPM and Hamamastu MPPC.

#### 6.3.3.4 Electronics and DAQ

**Front-end electronics ASIC:** High-density electronics is indispensable to instrumentation of high-granularity calorimetry. An ASIC chip named SPIROC, developed by the OMEGA group, is capable to handle 36 SiPMs. For each channel, it can be operated in

### NDL EQR-SiPM VS Hamamatsu MPPC

	NDL SiPM		Hamamatsu MPPC	
<b>Effective Active Area</b>	11-3030 B-S	22-1414 B-S	S13360-3025PE	S13360-1325PE
	3.0×3.0 mm <sup>2</sup>	1.4×1.4 mm <sup>2</sup> (2×2 Array)	3.0×3.0 mm <sup>2</sup>	1.3×1.3 mm <sup>2</sup>
<b>Effective Pitch</b>	10 μm	10 μm	25 μm	25 μm
<b>Micro-cell Number</b>	90000	19600	14400	2668
<b>Fill Factor</b>	40%	40%	47%	47%
<b>Breakdown Voltage (<math>V_b</math>)</b>	23.7±0.1V	23.7±0.1V	53±5V	53±5V
<b>Measurement O vervoltage (V)</b>	3.3	3.3	5	5
<b>Peak PDE</b>	27%@420nm	35%@420nm	25%@450nm	25%@450nm
<b>Max. Dark Count (kcps)</b>	< 7000	<1500	1200	210
<b>Gain</b>	$2\times10^5$	$2\times10^5$	$7.0\times10^5$	$7.0\times10^5$
<b>Temp. Coef. For <math>V_b</math></b>	17mV/° C	17mV/° C	54mV/° C	54mV/° C

**Figure 6.54:** Performance compare between EQR SiPM and Hamamatsu MPPC with similarly high micro-cell density.

an auto-trigger mode and has a dual-gain charge preamplifier with high dynamic range. It allows to measure for each channel the charge from 1 to 2000 photo-electron and the time within 1 ns using a 12-bit digitizing circuit. With one 8-bit 5V input DAC per channel, the bias voltage for each SiPM can be adjusted to reach its optimum. In each channel, there are 16 analogue memory cells that can buffer both charge and timing signals to be digitized afterwards consecutively. The digitization circuit is shared for both charge and timing measurements to minimize the power consumption, which needs to be as low as 25  $\mu W$  per channel. The latest version SPIROC2E has been improved in many aspects and its packaging has changed to a thinner BGA, which ensures a compact design for HBU and allows better automated mass soldering.

**HCAL Base Unit:** A merit of the AHCAL electronics is flexibility. One full AHCAL active layer can be constructed by connecting several base units (namely HBUs) via connectors, each with  $12 \times 12$  channels in a square plate of  $36 \times 36\text{ cm}^2$ . The exact granularity is being optimized for CEPC to balance between the detector performance and the number of total channels. To achieve a compact HCAL design, the PCB for each HBU should be thin enough and a 6-layer PCB within 1 mm thickness is proved to be feasible.

As a semiconductor detector, SiPM is intrinsically sensitive to environmental changes, especially temperature. Thus each SiPM needs on-site calibration, which requires an on-board LED circuit for each channel. There is an LED circuit at each channel of an HBU, which can emit UV light to a scintillator tile. Using these photons, the gain of a SiPM can be extracted and monitored.

**Detector interface:** ASIC chips are controlled by an interface board named DIF (Detector Interface). One DIF board handles a full HCAL active layer (a long slab with up to  $6 \times 3$  HBUs), corresponding to 72 ASICs in total. The expected data rate per DIF can be estimated based on the event rate at HCAL, which depends on the beam structure at CEPC.

**LED calibration board:** A dedicated LED calibration board is needed to control all LED circuits in an HCAL active layer. It can send trigger signals for the proper SiPM calibration.

**Power board:** SiPM operation relies on a proper reversely bias voltage. Therefore, between power supplies and ASIC chips, a power board is required to distributing the bias voltage to each SiPM. This power board can also play an important role in regulating voltages for protection and smooth working of SiPMs. Like the DIF board, it would be feasible to use only one such board for an active HCAL layer (up to  $6 \times 3$  HBUs).

### 6.3.3.5 DAQ system

**DAQ hardware:** DAQ system is also required to be compatible to the final detector layout, where two hardware parts are essential. One part is so-called LDA (Link to Data Aggregator), which collects all the data via DIFs from active layers in an HCAL segment and transmit them to a back-end PC for further processing or storage. Smart units like FPGAs are equipped on this board for data packaging and transmission. Modern FPGAs integrated with RAMs are an ideal option to have a capability of data buffering and some advanced feature like system on chip.

The other key hardware part is so-called CCC (Clock and Control Card), which provide a global clock signal and synchronize DIFs. Control signals are also sent to DIFs including starting and stopping acquisition.

**DAQ software:** The DAQ software is being developed in the framework of EUDAQ supported by AIDA2020, aiming for a generic solution for a combined setup with several detectors, which is important in test-beam activities during the prototyping phase. The latest version EUDAQ2 has made much progress during extensive beam tests for various combinations of detectors and can be considered as a solution for further HCAL prototyping and beam-test campaigns for CEPC.

## 6.4 Dual-readout Calorimetry

### 6.4.1 Introduction

Till now, the performance obtained in hadronic energy measurements has been by far worse than for the electromagnetic ones, since showers from single hadrons or jets develop an electromagnetic component (*em* fraction,  $f_{em}$ ), from  $\pi^0$  and  $\eta$  production, that exhibits large event-by-event fluctuations and dependence on the particle type and energy [26].

As a matter of fact, the *em* fraction changes as a function of the particle initiating the shower (e.g.,  $\pi$ ,  $K$ ,  $p$ ) since, for example, impinging  $\pi^\pm$  mesons can undergo a charge-exchange reaction with a nucleon as first interaction and generate a pure *em* shower, while a  $p$  can't do that.

Moreover, since  $\pi^0$  production happens at any stage of shower development, the  $f_{em}$  increases with the energy as well as with the depth ("age") of the shower.

The *em* and *non – em* components of a hadronic shower are normally sampled with very different sensitivity, producing large differences in the measured signals, heavily affecting the energy resolution capability.

To overcome the problem two methods have been exploited: compensation and dual readout (DR). The first relies on equalising the detector response to electromagnetic and

non-electromagnetic shower particles but requires the integration of the signals over large volumes (and long time) and leads to limited resolution for electromagnetic showers. The DR method allows to avoid these limitations by measuring and accounting for the  $f_{em}$ , on event-by-event basis. The showers are sampled through two independent processes, namely scintillation and Čerenkov light emissions. The former is sensitive to all ionizing particles, while the latter is produced by highly relativistic particles only, almost exclusively found inside the  $em$  shower component. By combining the two measurements, energy and  $f_{em}$  of each shower can be simultaneously reconstructed. The performance in hadronic calorimetry may be boosted toward its ultimate limit.

Over the last 15 years, the DREAM/RD52 collaboration at CERN has deeply investigated both homogeneous and sampling DR solutions [27]. The first don't suffer from sampling fluctuations and have, in principle, much higher light yields.

Nevertheless, the two signals are mixed together and must be separated by means of optical filters and/or timing properties. Last but not least, the cost of building a fully-homogeneous hadronic calorimeter looks prohibitive.

On the other hand, in sampling calorimeters, the two signals (from scintillation and Čerenkov light) are separated by construction since they are measured in independent detector elements. The results obtained so far show that a sampling fibre calorimeter may reach resolutions close to  $10\%/\sqrt{E}$  for  $em$  showers and better than  $\sim 30 - 40\%/\sqrt{E}$  for hadronic showers, coupled with strong standalone particle-ID capabilities. This allows  $W \rightarrow jj$  separation from  $Z \rightarrow jj$  by invariant mass, high-precision missing  $\nu$  three-vector by subtraction,  $e\text{-}\mu\text{-}\pi$  separation and tagging.

The intrinsic high granularity, exploited with Silicon Photo-Multipliers (SiPM) single-fibre readout, may as well provide powerful input to particle flow algorithms.

Indeed, while the DR concept has been extensively proven and experimentally validated in a series of beam tests, the use of standard Photo-Multiplier (PM) tubes to read out the Čerenkov and scintillation light has so far limited its development towards a full-scale system compliant with the integration in a particle detector at a colliding beam machine. These limitations can be overcome using SiPM, low-cost solid-state sensors of light with single photon sensitivity, magnetic field compliance and design flexibility. Concerning devices built on materials other than silicon, a relevant advantage in the detection of the Čerenkov light could in principle come from the development of sensors based on Silicon Carbide (SiC), essentially because of its UV sensitivity and visible-light blindness.

#### 6.4.2 Dual-Readout Calorimetry

The independent sampling of hadronic showers, through scintillation and Čerenkov light emission, allows to fully reconstruct, at the same time, energy and  $f_{em}$  of hadronic showers. In fact, the total detected signals, measured with respect to the electromagnetic energy scale, can be expressed as:

$$S = E [ f_{em} + \eta_S \cdot (1 - f_{em}) ] \quad (6.5)$$

$$C = E [ f_{em} + \eta_C \cdot (1 - f_{em}) ] \quad (6.6)$$

where  $\eta_S = (e/h)_S$  ( $\eta_C = (e/h)_C$ ) is the relative yield of the scintillation (Čerenkov) signal for the  $em$  to the hadronic component of the shower. The system can be easily solved giving:

$$\frac{C}{S} = \frac{[f_{em} + \eta_C \cdot (1 - f_{em})]}{[f_{em} + \eta_S \cdot (1 - f_{em})]} \quad (6.7)$$

$$E = \frac{S - \chi C}{1 - \chi} \quad (6.8)$$

where:

$$\chi = \frac{1 - \eta_S}{1 - \eta_C} = \cot \theta \quad (6.9)$$

This is the simplest formulation of hadronic calorimeter response: an *em* part with relative response of unity, and a *non-em* part with relative response  $\eta$ .

There are two unknowns for each shower,  $E$  and  $f_{em}$ , and two measurements S and C. The electromagnetic fraction,  $f_{em}$ , is determined entirely by the ratio C/S, and the shower energy calculated as in Eq. (4). Both C and S ( $e/h$ ) ratios have event-by-event fluctuations and should be considered stochastic variables, nevertheless the average  $\langle e/h \rangle$  values are essentially independent of hadron energy and species [28–30]. The global parameter  $\chi$  can be extracted with a fit to calibration data:

$$\chi = \frac{E_0 - S}{E_0 - C} \quad (6.10)$$

$$S = (1 - \chi)E_0 + \chi C \quad (6.11)$$

where  $E_0$  is the beam energy.

The geometrical meaning of the  $\theta$  angle can be understood by looking at the scatter plot of C versus S signals. In Figure 6.55, there are both (a) a prediction for the normalised scatter plot for protons and pions, and (b) the observed scatter plot for 60 GeV pions, in the RD52 lead/fibre calorimeter.

The plot in Figure 6.55(b) shows the data points located on a locus, clustered around a line that intersects the C/S = 1 line at the beam energy of 60 GeV.  $\chi$  is the energy-independent slope of the event locus. This is to be expected. In first approximation, the signal generated in the Čerenkov fibers is produced only by the *em* components of the hadron showers. The larger the *em* fraction  $f_{em}$ , the larger the C/S signal ratio. Events in which (almost) the entire hadronic energy is deposited in the form of *em* shower components give signals very similar to those from 60 GeV electrons and are, therefore, represented by data points located near (S=60, C=60) in the plot.

All signals are relative to the *em* scale meaning that both the Čerenkov and the scintillation responses have to be calibrated with electrons only, i.e. no hadronic calibration is required. This is one of the most qualifying point of dual-readout calorimetry.

The effectiveness of this approach has been probed by the DREAM/RD52 collaboration over a 15-year research program with a variety of detector solutions. Results and simulations [31–36] provide, so far, confidence that a fibre-sampling calorimeter, even without longitudinal segmentation, may meet the requirements of the CepC physics programme in a cost-effective way. Linearity and energy resolution, for both *em* and hadronic showers,  $e/\pi/\mu$  separation, spatial resolution, all show adequate performance.

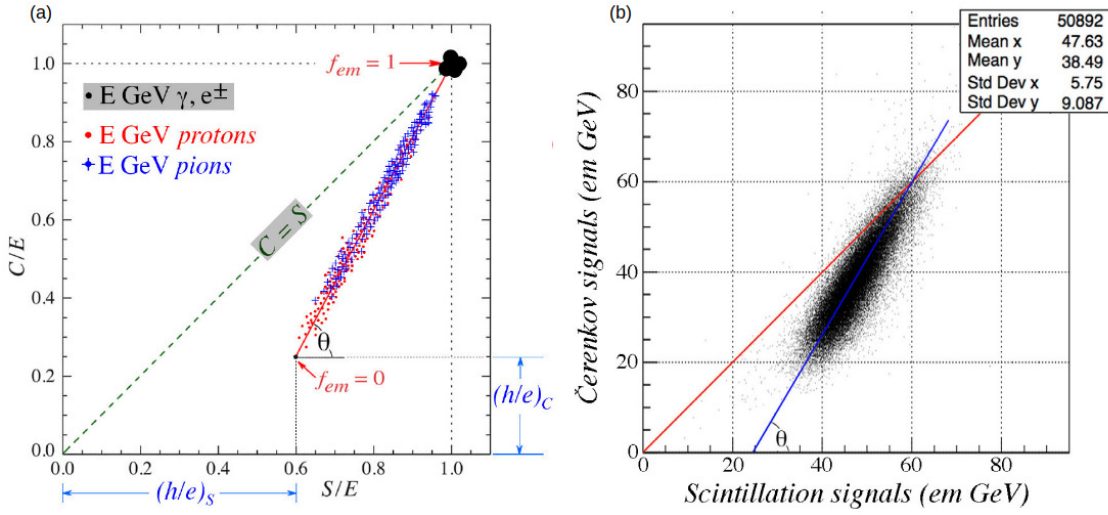


**Figure 6.55:** (a) Scatter plot of  $C/E$  versus  $S/E$  in a dual-readout calorimeter for  $p$  and  $\pi$ ; (b) scatter plot of  $C$  versus  $S$  signals for 60 GeV pions in the RD52 dual-readout lead/fibre calorimeter.

### 6.4.3 Layout and Mechanics

#### 6.4.3.1 Layout

A possible projective layout has been studied by the 4th Detector Collaboration and described in its LoI [37]. Assuming the converter to be copper, the calorimeter is a copper matrix loaded with 1 mm diameter, 1 mm apart, alternate scintillating and clear (for Čerenkov light detection) fibres. About 200 cm ( $10 \lambda$ ) long, projective towers cover (at  $\theta \sim 90^\circ$ ) about  $1.4^\circ$  in both  $\phi$  and  $\theta$ , with of the order of 2000 fibres per tower. The dimensions of the inner faces in the barrel section depend on  $\theta$ , and increase going in the forward direction. The sampling fraction is kept constant by fibres starting at different depths inside each tower.

This layout has been already imported in the simulations for the CepC detector and will be validated in the next months.

#### 6.4.3.2 Mechanics (Material Choice and Machining)

Both lead and copper have been used as absorber materials by the DREAM/RD52 collaboration. Their main properties are:

$$\text{Lead : } \rho = 11.3 \text{ g/cm}^3, X_0 = 0.56 \text{ cm}, \rho_{Mol} = 1.60 \text{ cm}, \lambda_{int} = 170 \text{ mm} \quad (6.12)$$

$$\text{Copper : } \rho = 8.96 \text{ g/cm}^3, X_0 = 1.44 \text{ cm}, \rho_{Mol} = 1.56 \text{ cm}, \lambda_{int} = 151 \text{ mm} \quad (6.13)$$

meaning that, for hadronic showers, a full-coverage solution with lead will give broader and longer showers and a total mass 42% heavier than using copper. A full-containment  $3 \times 3 \times 10 \lambda^3$  prototype will need about 5 tons of material with lead and 2.8 tons with copper.

An even stronger reason in favour of copper is the fact that, being the Čerenkov light almost exclusively produced by the  $em$  shower components and the (e/mip) ratio 50% higher for copper than for lead, the Čerenkov light yield should be significantly higher in copper, resulting in a better hadronic resolution.

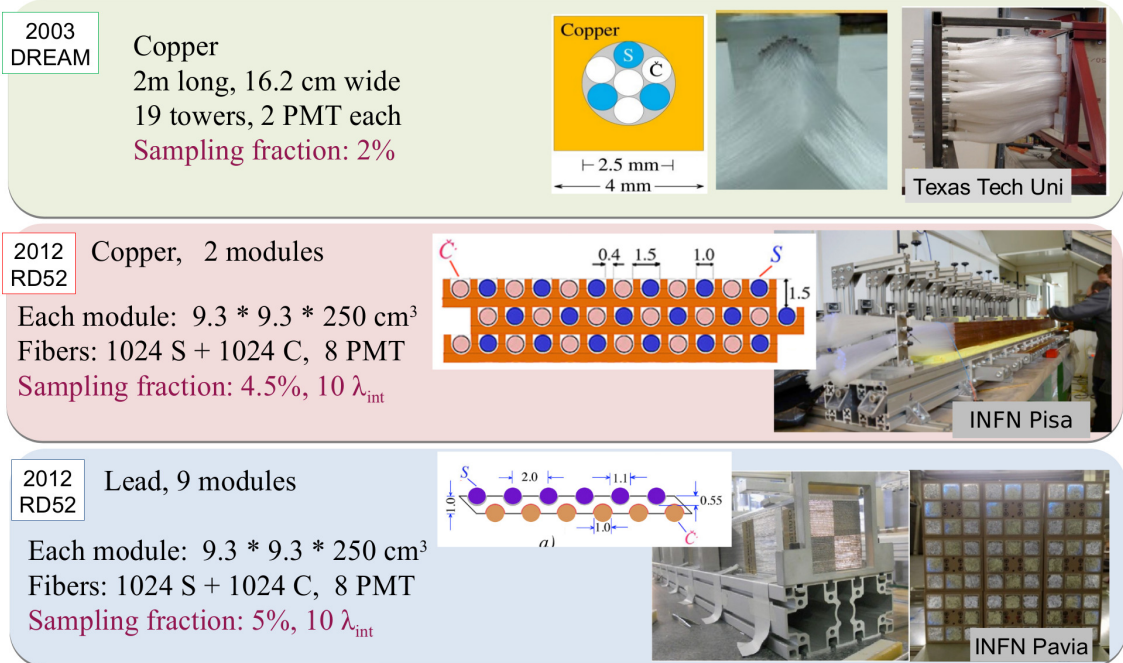


**Figure 6.56:** The DREAM calorimeter (top), built in 2003, and the RD52 prototypes, with copper (middle) and lead (bottom), built in 2012.

On the other hand, copper extrusion, with the required tolerances in planarity and groove parallelism, is not yet an established industrial process. A variety of techniques (extrusion, rolling, scraping and milling) for machining the converter layers have been tested, essentially by John Hauptman and collaborators at Iowa State University and by Fabrizio Scuri at INFN-Pisa. None has been qualified for a large-scale production and identifying an industrial and cost-effective process, including moulding, is a relevant issue.

In the 3-year R&D INFN program, under discussion, the identification of an industrial procedure to produce the converter layers is one key point.

Alternative copper alloys (brass, bronze) will be investigated as well, both for addressing the production process issues and for optimising the detector performance.

#### 6.4.4 DREAM/RD52 Prototype Studies

Different prototypes were built and studied by the DREAM/RD52 collaboration, with copper or lead as absorber. A summary of the most significant results [31–36] is given, in particular for the matrices built in 2012: a matrix of 9 lead modules and a matrix of 2 copper modules, each module  $9.3 \times 9.3 \times 250 \text{ cm}^3$  (see Figure 6.56 for the mechanical details, the first DREAM calorimeter built in 2003 is also shown on the top). From the readout point of view, the calorimeter was arranged as in Figure 6.57.

##### 6.4.4.1 Electromagnetic Performance

In Figure 6.58 the linearity of the response for both matrices is shown. The range of measurement is different for the two (spanning 6-60 GeV for Cu and 60-150 GeV for Pb). The deviations for the very first points ( $\lesssim 10 \text{ GeV}$ ) are likely due to the spread of the energy of the beam particles.

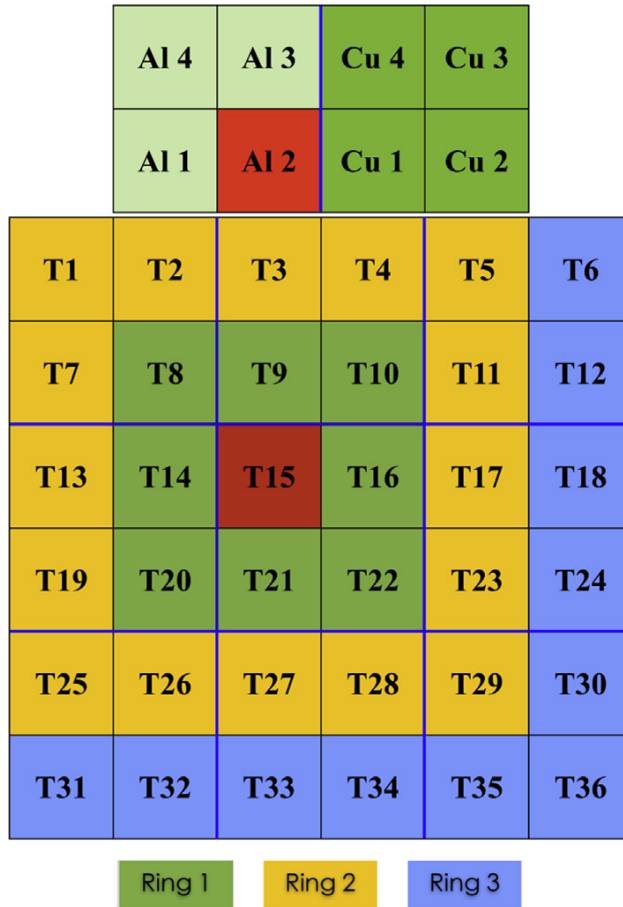


**Figure 6.57:** The RD52 calorimeter as tested at the end of 2012. It consisted of 9 lead-based modules, each consisting of 4 towers (towers 1–36), and 2 copper-based modules, placed on top of the lead array. Each tower was readout by two photomultipliers, one for scintillation and one for Čerenkov light detection. The left copper module (of which the towers are marked as “Al”) was equipped with Čerenkov fibres with an aluminised upstream end face. For the measurements described in this paper, the particle beams were typically steered in the center of tower T15.

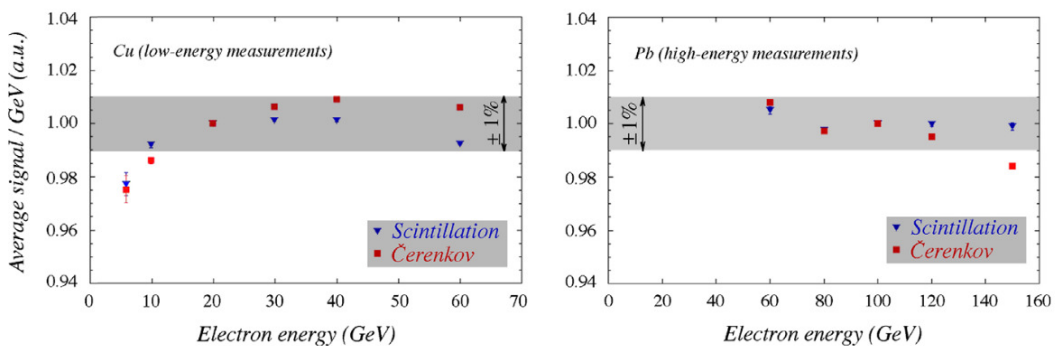


**Figure 6.58:** The linearity of the copper (left) and lead (right) based fibre calorimeters for em shower detection in the scintillation and Čerenkov channels.

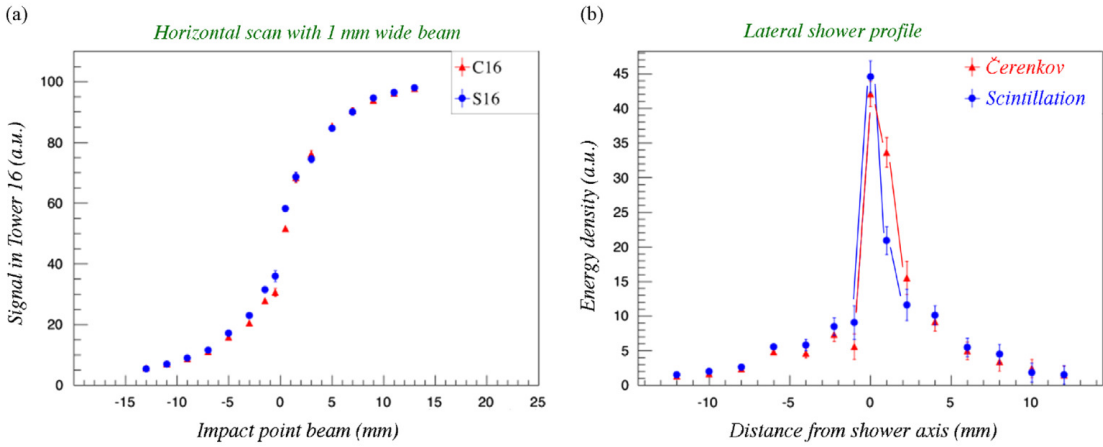


**Figure 6.59:** The signal from a 1 mm wide beam of 100 GeV electrons, as a function of the impact point (a), and the lateral shower profiles derived from this measurement (b).

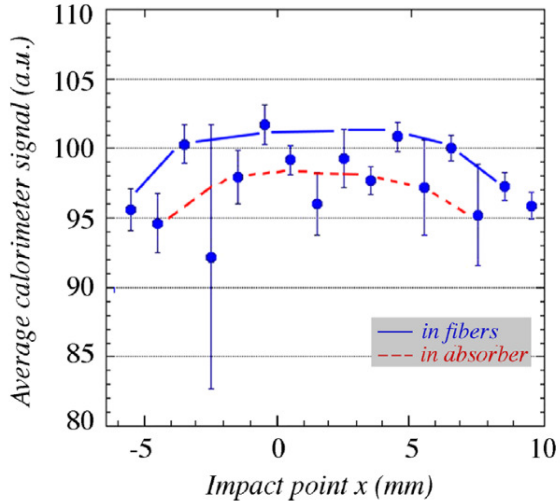


**Figure 6.60:** The scintillation signal for 100 GeV electrons developing showers in the lead matrix as a function of the beam impact point.

Figure 6.59 shows the radial shower profile and the sensitivity to the impact point: the core of the signal spans just few mm. Figure 6.60 shows the dependence of the S signal on the impact point for particles entering parallel to the fibres. This introduces a constant term in the resolution that can be avoided with a small tilt of the fibre axis. In the C fibres, the problem doesn't show up since the early (collimated) part of the shower produces photons outside the numerical fibre aperture.

For the reconstruction of the energy of *em* showers, C and S signals provide independent uncorrelated measurements, with different sensitivity of the response. They are affected by different problems: S signals have a photo-electron statistics of at least one order of magnitude higher than C signals, and their fluctuations are largely dominated by the sampling fluctuation of the energy deposits. C signal fluctuations are generally dominated by the limited photo-electron statistics, especially at low energies. Nevertheless, for C signals, the constant term is negligible giving a better resolution at high energies. Averaging the two measures improves the resolution up to a factor of  $\sqrt{2}$ . Separate and

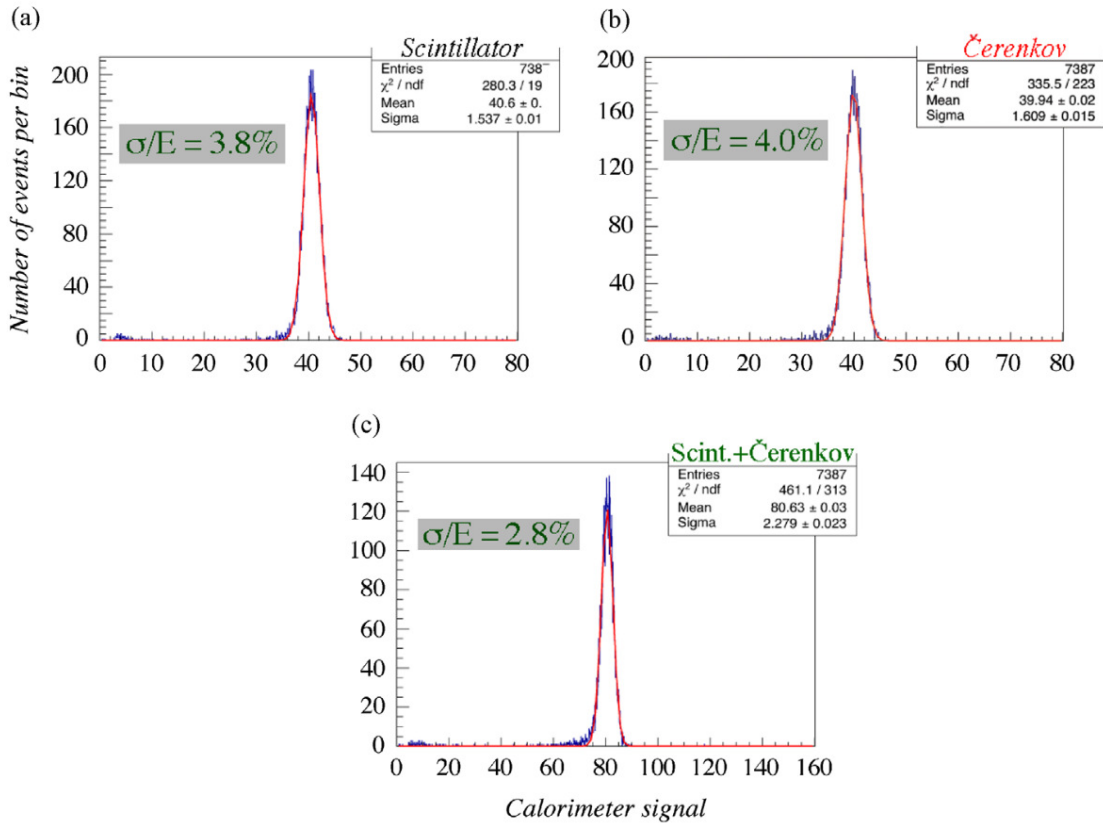


**Figure 6.61:** Signal distributions for 40 GeV electrons in the copper-fibre calorimeter: from the sum of the scintillating fibres (a), of the Čerenkov fibres (b), of all fibers (c). The angle of incidence of the beam particles ( $\theta$ ,  $\phi$ ) was  $(1.5^\circ, 1.0^\circ)$ . The size of the beam spot was  $10 \times 10 \text{ mm}^2$ .

combined (unweighted) results for the copper matrix are shown in Figure 6.61 for 40 GeV electrons.

In Figure 6.62, the electromagnetic resolution is shown for the 2 matrices.

#### 6.4.4.2 Hadronic Performance

The RD52 lead matrix response was studied with pion and proton beams [36]. High-multiplicity events ("jets") were also generated by means of a target. The energy was reconstructed with the dual-readout relation (Eq. 4), that restores a gaussian behaviour and linearity of the response (Figure 6.63 and Figure 6.64).

The comparison of  $p$  and  $\pi$  signals at 80 GeV is shown in Figure 6.65, confirming that the method largely compensates for the differences in shower composition.

The limited lateral size of the matrix (about  $1 \lambda$ ) allows to collect, in average,  $\sim 90\%$  of the shower energy so that leakage fluctuations dominate the resolution capability. Leakage counters were used to select events about fully contained (that of course, tend to have a higher  $f_{em}$ ). The resolution improves by a factor of almost 2 in this case (Figure 6.66). A second effect affecting resolution is the light attenuation in the fibres, that causes early starting showers to be observed at lower signal values. The hadronic resolution, to be corrected for both effects, was reconstructed to be  $\sim 70\%/\sqrt{E}$ .

Geant4 simulations point at a possible resolution of  $\sim 30\%/\sqrt{E}$ , allowing sensible separation of the  $W/Z$  decays to jet pairs (Figure 6.68). The figure summarizes the situ-

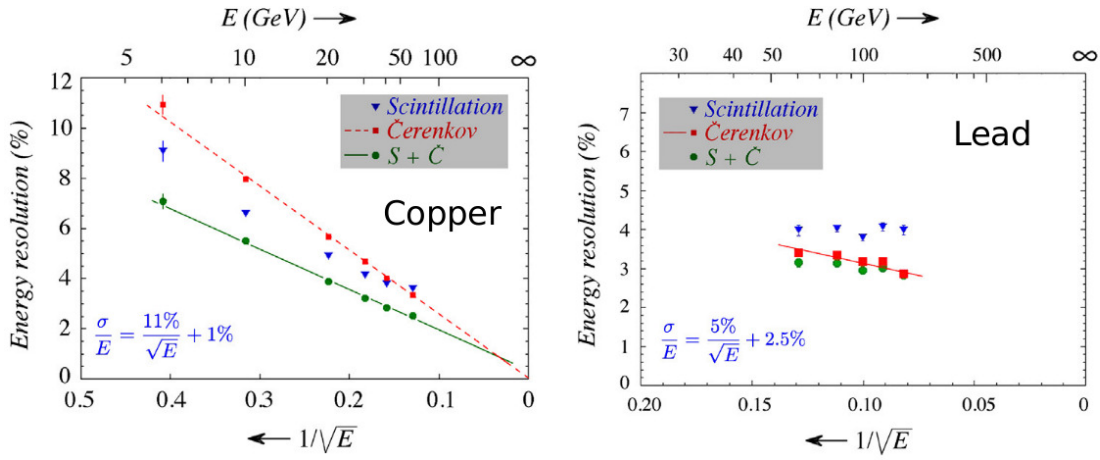


**Figure 6.62:** The energy resolution for electrons in the copper-fibre module (left) and in the lead-fibre module (right), as a function of the beam energy. Shown are the results for the two types of fibres, and for the combined signals. The angle of incidence of the beam particles ( $\theta$ ,  $\phi$ ) was ( $1.5^\circ$ ,  $1.0^\circ$ ). The size of the beam spot was  $10 \times 10 \text{ mm}^2$ .

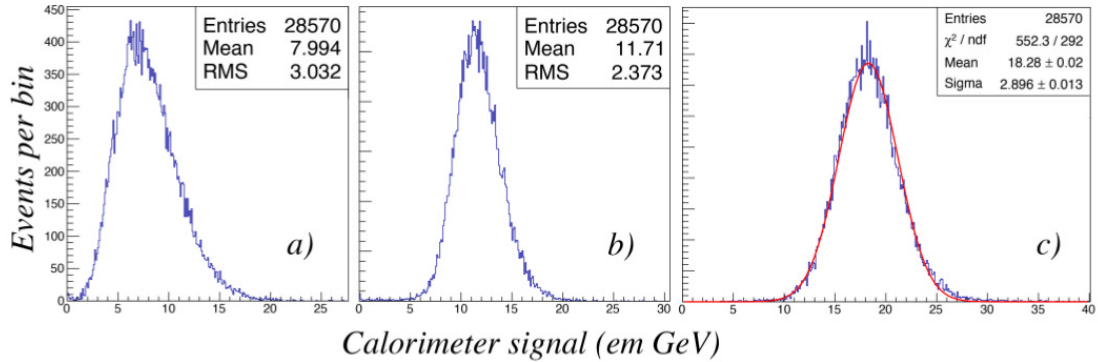


**Figure 6.63:** Signal distributions for  $20 \text{ GeV } \pi^-$  particles. Shown are the measured Čerenkov (a) and scintillation (b) signal distributions as well as the signal distribution obtained by combining the two signals according to Equation 4, with  $\chi = 0.45$  (c).

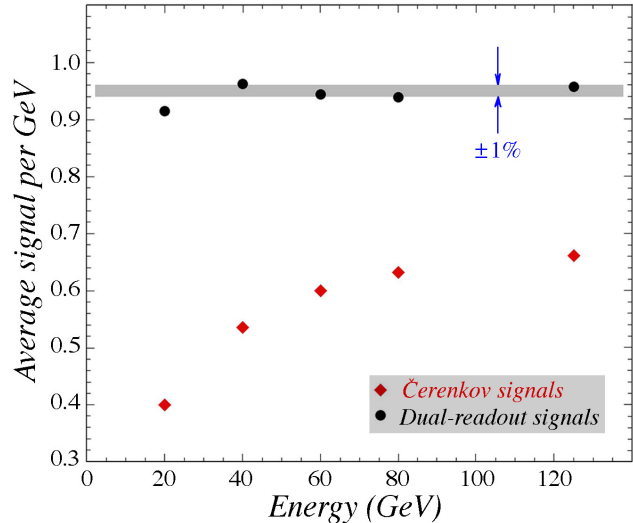


**Figure 6.64:** The hadronic response for single pions. Shown are the average Čerenkov signal and the dual-readout signal (Eq. 4) per unit deposited energy, as a function of the pion energy.

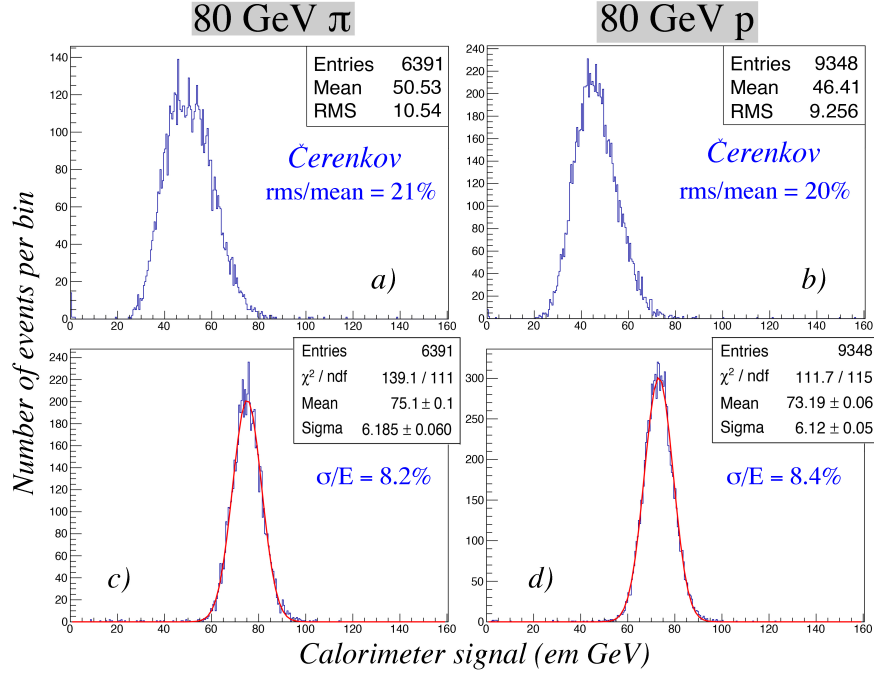


**Figure 6.65:** Signal distributions for the Čerenkov signals from 80 GeV  $\pi^+$  (a) and protons (b), as well as the dual-readout total signals for 80 GeV  $\pi^+$  (c) and protons (d).

ation concerning the hadronic energy resolution, for single pions. Experimental data on hadronic performance compared to GEANT4 simulations are shown in Figure 6.68(a). The experimental data obtained with the original DREAM fibre calorimeter, which had a lateral cross-section of  $820 \text{ cm}^2$ , are compared [35] with simulations using the standard FTFP\_BERT hadronic simulation package for the geometry of that detector. The improvement expected for a larger detector ( $65 \times 65 \text{ cm}^2$  lateral cross-section) with the RD52 geometry is also shown, both for the standard FTFP\_BERT package and for the high-precision version of this package. For comparison, the record setting experimental data reported by SPACAL [38] are also shown, as well as a curve representing an energy resolution of  $30\%/\sqrt{E}$ .

#### 6.4.4.3 $e/\pi$ Separation

Four discriminating variables were identified for implementing  $e/\pi$  separation: the fraction of energy in the central tower, the Čerenkov/scintillation light signal ratio, the signal starting time, the total charge/amplitude ratio, shown in Figure 6.69. A multivariate neural network analysis showed that the best  $e/\pi$  separation achievable for 60 GeV beams was 99.8% of electron identification efficiency with 0.2% pion misidentification. Further improvements may be expected by including the full time structure information of the pulses, especially if the upstream ends of the fibers are made reflective.

#### 6.4.5 Sensors and Readout Electronics

Separately read out the signals from the Čerenkov and scintillation fibre forest and avoid oversampling of late developing showers is an issue that may be successfully addressed through the use of Silicon Photo-Multipliers (SiPM), allowing the separate reading of each fibre and magnetic field insensitivity. This, in principle, assuming powering and cooling

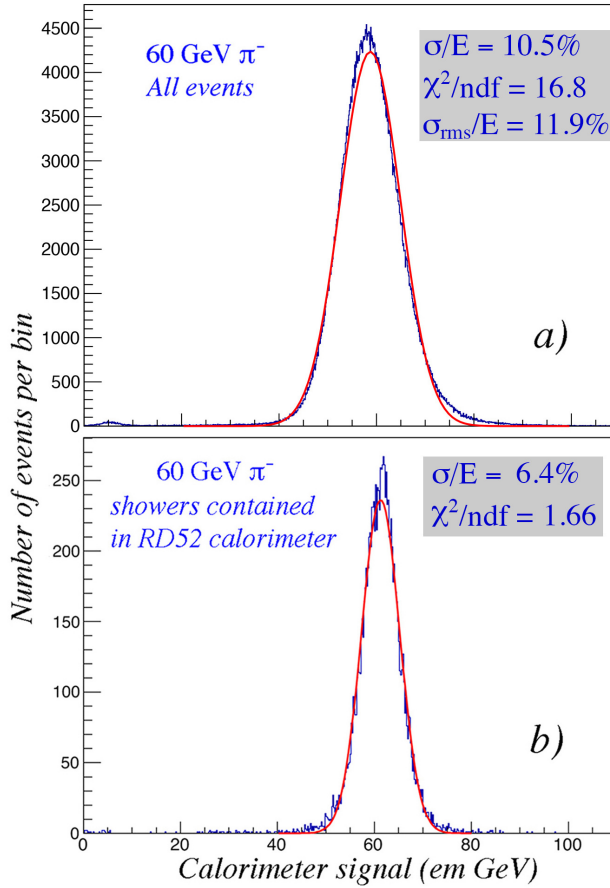


**Figure 6.66:** Total signal distributions for 60 GeV  $\pi^-$ ? , measured with the dual-readout method. Shown are the distributions for all events (a) and for events fully contained inside the calorimeter, i.e., for which no energy leakage was measured in the leakage counters (b).

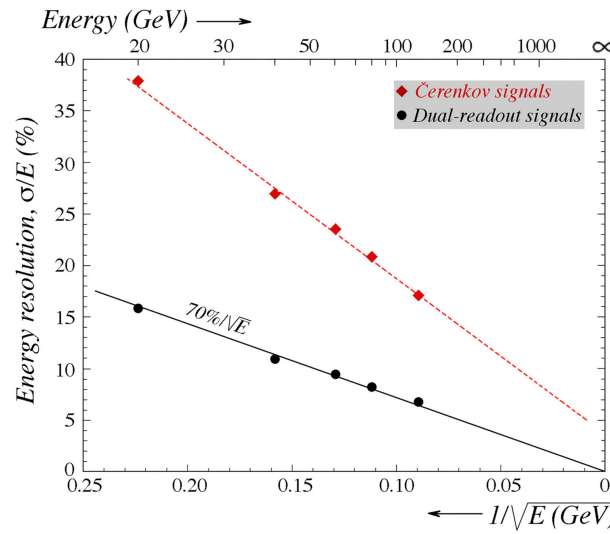


**Figure 6.67:** The hadronic energy resolution of the RD52 lead-fibre dual-readout calorimeter, for single pions. Shown are the results for the Čerenkov signals alone, and for the dual-readout signals.

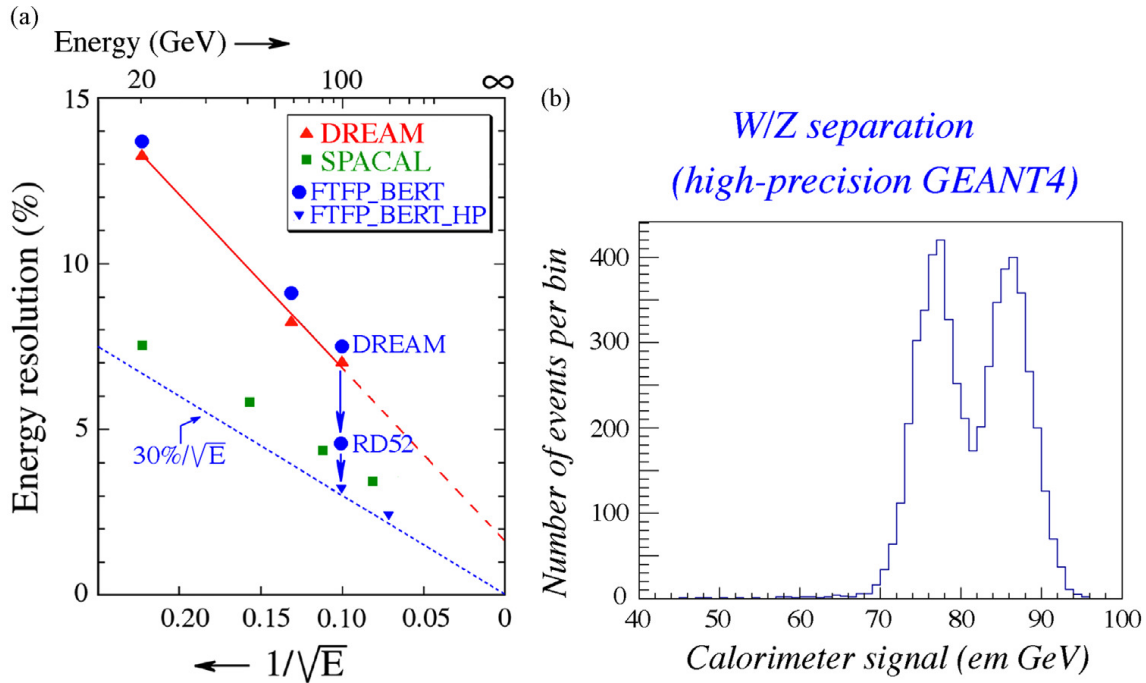


**Figure 6.68:** Experimental data on hadronic performance compared to Geant4 simulations (a). See text for details. Diagram (b) shows the results of a simulation for a mixture of hadrons with the energies of the W and Z vector bosons, using the high-precision hadronic shower simulation package.

don't pose issues, allows for a transversal segmentation as small as possible. SiPM are low-cost solid state light sensors with single photon sensitivity that underwent an impressive development over the last years. Tests done in the last 2 years by the RD52 collaboration show that effective solutions for small scale prototypes are very close already now. Thanks to their higher photon detection efficiency wrt standard PM, the Čerenkov light signal should be improved with a gain in the resolution for hadronic showers. On the other hand, the scintillation light spans a very large dynamic range and saturation and non-linearity effects were observed already for low-energy *em* showers. In Figure 6.70, the number of photoelectrons per GeV measured in July 2017, with a very small module ( $1\text{cm}^2$  section,  $32 + 32$  fibres) is shown. The most relevant technical specifications of the sensors were  $1600$ ,  $25 \times 25 \mu\text{m}^2$ , cells, and a  $25\%$  nominal detection efficiency.

C signals show a linear response with about  $30$  p.e./GeV while S signals shows a decreasing sensitivity starting at around  $1000$  p.e./GeV, for  $10$  GeV electron showers. It should be mentioned the fact that the shower containment is around  $40\%$ . Last but not least, the problem of serious light leaks of the S signals to the neighbouring C SiPM, observed in the first 2016 tests, looks solved thanks to a staggered readout of the C and S fibres (Figure 6.71).

#### 6.4.5.1 Sensor Choice

As far as the scintillation light detection is concerned, saturation or non linearity should largely disappear with higher density devices (e.g. with  $10000$ ,  $10 \times 10 \mu\text{m}^2$ , cells). The definition of the optimal dynamic range and the qualification of existing silicon photomultipliers in that regard, will be likely addressed in a short-term *R&D* phase.

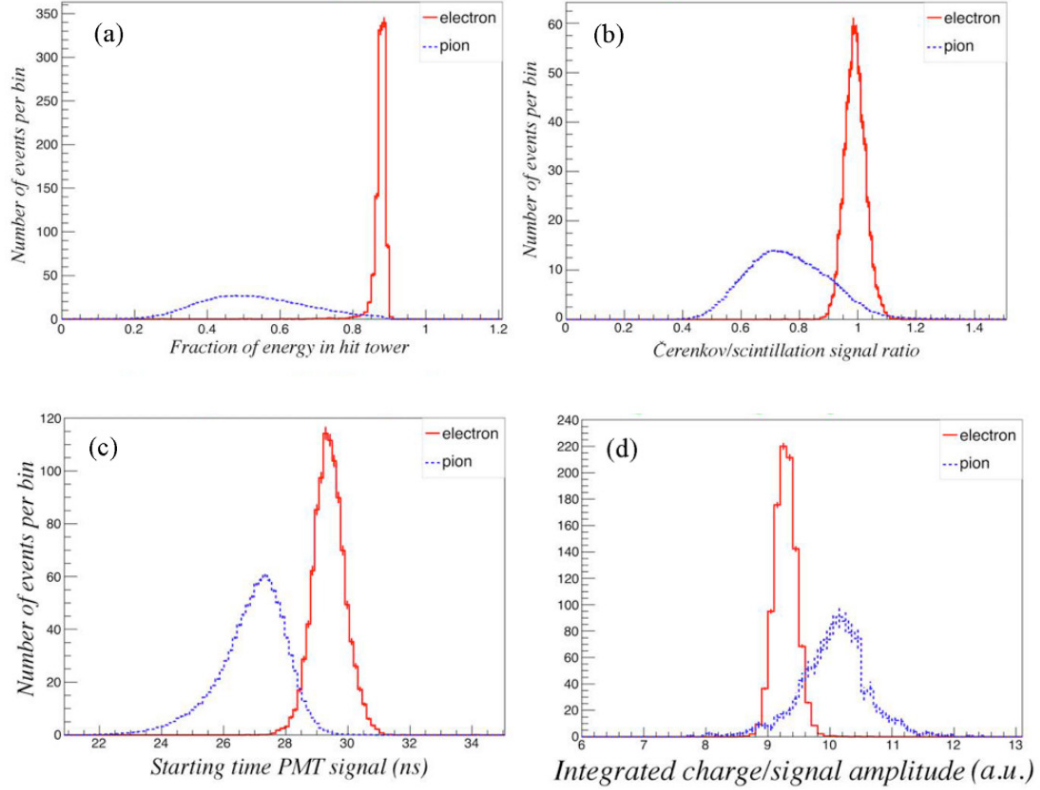


**Figure 6.69:** Distribution of four discriminating variables: energy fraction deposited in the hit tower for the (a), C/S signal ratio in the hit tower (b), starting time of the PM signal (c), ratio of the integrated charge and the amplitude of the signals (d), for electron and pion showers.

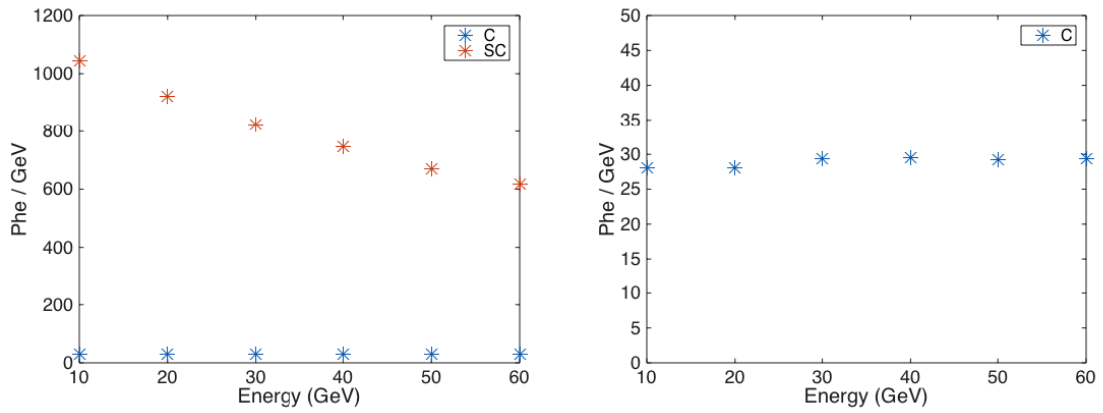


**Figure 6.70:** Number of photoelectrons per GeV for both the scintillation and the Čerenkov signals (left) and for the Čerenkov signal only (right), as a function of the electron energy. The main sensor specifications were 1600,  $25 \times 25 \mu\text{m}^2$ , cells, and a 25% nominal PDE.

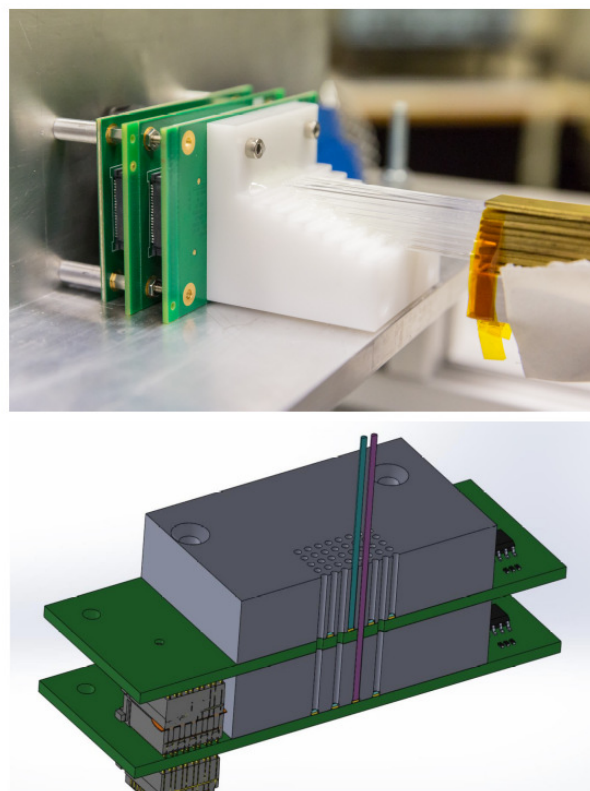


**Figure 6.71:** Staggered readout scheme: the scintillation and Čerenkov fibres are readout at different planes to avoid light leakage into neighbouring channels.

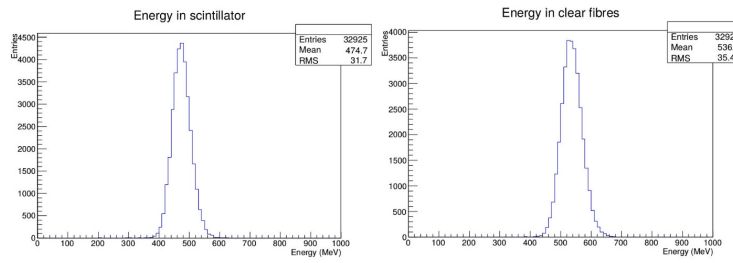


**Figure 6.72:** Energy deposited in scintillating (a) and Čerenkov (b) fibres, by 20 GeV electrons.

For the Čerenkov light, improvements of the photon collection may come with the development of Silicon Carbide (SiC) sensors, that are expected to provide exclusive UV sensitivity (i.e. visible-light blindness). It must be said that the R&D of these device is at a very early stage and they still miss a proof that they will really give a significant improvement in the Čerenkov light detection. A program for the development and qualification of SiC sensors is under discussion at INFN.

#### 6.4.5.2 Front-End Electronics and Readout

Concerning the front-end, the development shall certainly evaluate the use of Application Specific Integrated Circuits (ASIC), to handle and reduce the information to be transferred to the DAQ system. A major question is finding the optimal way for summing signals from a plurality of sensors into a single output channel. Available ASICs will have to be analysed, compared and qualified with the goal to select the optimal one and/or define the specification for a dedicated design to be pursued at a later stage. The development and usage of a feature-extracting processor has to be considered, in particular for addressing the problem of disentangling overlapping *em* and hadronic showers.

#### 6.4.6 Monte Carlo Simulations

Geant4 simulations (version 10.02.p01-10.03.p01, with FTFP\_BERT\_HP physics list) are under development and analysis for understanding the performance of both testbeam modules and a  $4\pi$  calorimeter integrated in a detector, with magnetic field, tracking and preshower elements.

##### 6.4.6.1 *em* Performance

A  $31 \times 31 \times 100 \text{ cm}^3$  Cu matrix, with 1 mm fibres at 1 mm distance, has been simulated for the evaluation of the electromagnetic performance. PMMA clear fibres and Polystirene scintillating fibres, with a 3% thick cladding ( $C_2F_2$  Fluorinated Polymer for clear and PMMA for scintillating fibres), were the sensitive elements.

A small ( $\lesssim 1^\circ$ ) tilt angle was introduced to avoid large non gaussian tails in the scintillation signal due to channeling and oversampling.

The energy containment for 20 GeV electrons was estimated to be  $\sim 43.4\%$ , with sampling fractions of 5.3% and 6.0% (see Figure 6.72), for scintillating and clear fibres, respectively.

Given the integral sampling fraction of about 11.3% and the 1 mm thick fibres, the contribution to the energy resolution due to sampling fluctuations can be estimated to be around:

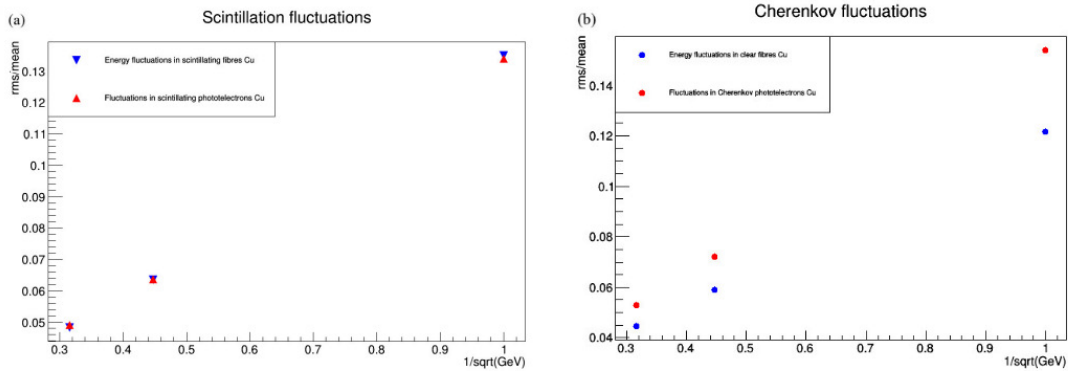


**Figure 6.73:** Relative fluctuation of the total signal detected in the scintillating (a) and Čerenkov (b) fibres, for both the energy deposit and the number of photoelectrons.

$$\frac{\sigma}{E} = 2.7\% \times \frac{\sqrt{1/0.113}}{\sqrt{E}} = \frac{8.0\%}{\sqrt{E}} \quad (6.14)$$

ultimate limit on the *em* resolution.

One of the main (blocking) issue was the cpu time needed for the light propagation up to the photodetectors, dominated by the scintillating photons. Nevertheless the analysis has shown that the fluctuations in the detection of the scintillating light (about 5500 photoelectrons/GeV) are largely dominated by the energy sampling fluctuations (Figure 6.73(a)). This is not true for the Čerenkov light signals (Figure 6.73(b)), which sensitivity is estimated to be of about 108 photoelectrons/GeV.

So, the propagation of the scintillation light has been switched off without biasing the detector performance while for the Čerenkov photons a parameterization has been introduced, convoluting the effect of the light attenuation, the angular acceptance and the Photon Detection Efficiency (PDE). The performance obtained in this way with a single thread over a 2.0 GHz processor ranges from  $\sim 11.3\text{s}$  at 40 GeV up to  $\sim 72\text{s}$  at 250 GeV.

In Figure 6.74 the resolutions are shown for both C and S signals, separately, and for the unweighted average value of the two.

The fit to the data points gives:

$$S \text{ only : } \frac{\sigma}{E} = \frac{10.1\%}{\sqrt{E}} + 1.1\% \quad (6.15)$$

$$C \text{ only : } \frac{\sigma}{E} = \frac{17.3\%}{\sqrt{E}} + 0.1\% \quad (6.16)$$

$$\text{combined : } \frac{\sigma}{E} = \frac{10.1\%}{\sqrt{E}} + 0.4\% \quad (6.17)$$

A slightly better result using a weighted average is under evaluation.

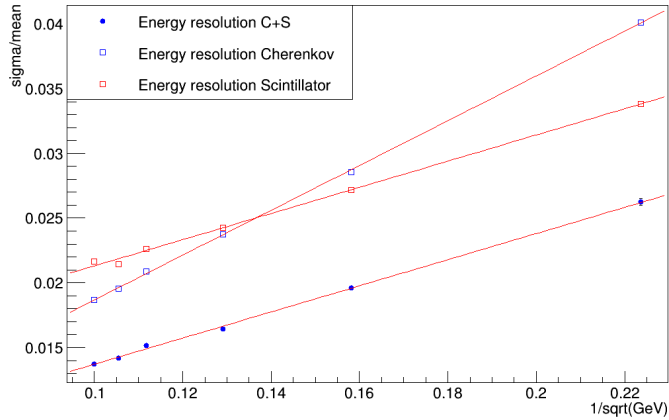


**Figure 6.74:** Relative resolution for  $em$  showers for the C and S signals, independently, and for the average of the two.

#### 6.4.6.2 Short Term Planning and Open Issues

The performance for single hadrons, jets and  $\tau.s$  has to be understood and the work has just started. For validation, the comparison with the data taken with the Pb matrix (the only recent prototype with a sensible hadronic shower containment) is planned.

About the  $em$  simulations, the priority will be the comparison with the 2017 testbeam data and the calibration of the absolute photoelectron scale for the Čerenkov light.

In general, an understanding of light attenuation effects is also needed, for a  $\sim 2 - 2.5m$  long detector, that affect the hadronic resolution as a function of the shower development point (late starting showers will give bigger and faster signals). The evaluation of pro/cons of filters (to dump the short attenuation-length components) and mirrors (to increase the number of photons that may reach the photodetectors) may be relevant in this context.

The effects of the integration of a preshower detector have to be evaluated and the  $e/\pi$  separation assessed and quantified, for both isolated particles and within jets.

About physics, a (non exhaustive) list of benchmark channels to be studied is:  $H \rightarrow \gamma\gamma$ ,  $H \rightarrow \tau\tau$ ,  $H \rightarrow gg$ ,  $Z \rightarrow jj$ ,  $W \rightarrow jj$ ,  $H \rightarrow ZZ^* \rightarrow 4j$ ,  $H \rightarrow WW^* \rightarrow 4j$ .

#### 6.4.7 Final Remarks

After a 15-year long research program on dual-readout calorimetry of the DREAM/RD52 collaboration, this technology looks mature for the application in future experimental programs. The results show that the parallel, independent, readout of scintillation and Čerenkov light, makes possible to cancel the effects of the fluctuations of the electromagnetic fraction of hadronic showers, dominating the energy resolution of most calorimeters built so far. In conjunction with high-resolution  $em$  and hadronic energy measurements, excellent standalone particle-id capability has been demonstrated as well.

Those results give increasing support to the conviction that a a matrix of alternating scintillating and clear fibres, inserted in copper strips and readout by Silicon PhotoMultipliers (SiPM), should be able to provide performance more than adequate for the physics programs at the proposed future CepC collider.

Nevertheless, there is a series of technical and physics issues that needs to be solved in order to arrive up to the design of a realistic  $4\pi$  detector. An INFN project, with a 3 year programme, is going to be discussed in the next weeks, aiming at addressing the main problems:

- a) The industrial machining of foils of copper (or some other material) with the required precision.
- b) The readout of the high granularity matrices of SiPM that, in order to be effective, will require the development of a dedicated Application Specific Integrated Circuit (ASIC). Possible aggregations of more fibre outputs into a single channel have also to be implemented and studied.
- c) The development of a modular solution and the assessment, at all levels, of its performance, through beam tests of small modules and simulations. An intensive program of simulations is already ongoing, with the target of the CepC CDR. The response to single particles and jets is under study, in standalone configurations. The work for understanding the behaviour of a calorimeter integrated in a full detector, with a tracking and a magnetic system, has also started. This will include, as well, the evaluation of the combined performance with a preshower detector in front.

## References

- [1] CALICE Wikipage.  
<https://twiki.cern.ch/twiki/bin/view/CALICE/>.
- [2] J.-C. Brient, *Improving the jet reconstruction with the particle flow method: An introduction*, 2004. Calorimetry in particle physics. Proceedings, 11th International Conference, CALOR 2004, Perugia, Italy.,
- [3] H. Videau and J. C. Brient, *Calorimetry optimised for jets*, in *Proc. 10th International Conference on Calorimetry in High Energy Physics (CALOR 2002), Pasadena, California* [39].
- [4] H. Videau and J. C. Brient, *A Si-W calorimeter for linear collider physics*, in *Proc. 10th International Conference on Calorimetry in High Energy Physics (CALOR 2002), Pasadena, California* [39], pp. 309–320.
- [5] CALICE Collaboration, R. Cornat, *Semiconductor sensors for the CALICE SiW EMC and study of the cross-talk between guard rings and pixels in the CALICE SiW prototype*, in *Proceedings CALOR'08*, vol. 160, p. 012067. 2009.
- [6] ILD Collaboration, T. Behnke et al., *International Linear Collider – Detector Baseline Document*, DESY / FERMILAB / CERN, 2013.  
<https://edmsdirect.desy.de/edmsdirect/file.jsp?edmsid=D00000001021295>.
- [7] CMS Collaboration, A. M. Magnan, *HGCAL: a High-Granularity Calorimeter for the endcaps of CMS at HL-LHC*, *JINST* **12** (2017) no. 01, C01042.
- [8] CMS Collaboration, A. Martelli, *The CMS HGCAL detector for HL-LHC upgrade*, in *5th Large Hadron Collider Physics Conference (LHCP 2017) Shanghai, China, May 15-20, 2017*. 2017. [arXiv:1708.08234 \[physics.ins-det\]](https://arxiv.org/abs/1708.08234).

- <http://inspirehep.net/record/1620207/files/arXiv:1708.08234.pdf>.
- [9] H. Zhao, *PFA Oriented ECAL Simulation and Geometry Optimization for the CEPC*, in *proceeding of the International Conference on Calorimetry for the High Energy Frontier (CHEF 2017)*. 2017.
- [10] D. Jeans, *Simalution of the SiW-ECAL for ILD*, in *proceedings of LCWS 2017*. 2017.
- [11] T. S. et al., *Performance study of SKIROC2/A ASIC for ILD Si-W ECAL*, in *proceeding of the International Conference on Calorimetry for the High Energy Frontier (CHEF 2017)*. 2017.
- [12] D. Grondin, J. Giraud, and J.-Y. Hostachy, *CALICE Si/W ECAL: Endcap structures and cooling system*, in *Proceedings, International Workshop on Future Linear Colliders 2016 (LCWS2016): Morioka, Iwate, Japan, December 05-09, 2016*. 2017. [arXiv:1702.03770 \[physics.ins-det\]](https://arxiv.org/abs/1702.03770).  
<http://inspirehep.net/record/1513187/files/arXiv:1702.03770.pdf>.
- [13] V. Boudry, *SiW ECAL R&D*, in *Fourth International Workshop on Future High Energy Circular Colliders (CEPC2014)*. 2014.  
<http://indico.ihep.ac.cn/event/4338/session/2/contribution/35/material/slides/0.pdf>.
- [14] CALICE Collaboration, J. Repond et al., *Design and Electronics Commissioning of the Physics Prototype of a Si-W Electromagnetic Calorimeter for the International Linear Collider*, *JINST* **3** (2008) P08001, [arXiv:0805.4833 \[physics.ins-det\]](https://arxiv.org/abs/0805.4833).
- [15] C. Adloff et al., *Response of the CALICE Si-W electromagnetic calorimeter physics prototype to electrons*, *Nucl. Instrum. Meth.* **A608** (2009) 372–383.
- [16] CALICE Collaboration Collaboration, R. Poschl, *A large scale prototype for a SiW electromagnetic calorimeter for a future linear collider*, in *Proceedings of International Workshop on Future Linear Colliders (LCWS11) 26-30 Sep 2011. Granada, Spain*. 2012. [arXiv:1203.0249 \[physics.ins-det\]](https://arxiv.org/abs/1203.0249).
- [17] V. Balagura et al., *SiW ECAL for future  $e^+e^-$  collider*, in *Proceedings, International Conference on Instrumentation for Colliding Beam Physics (INSTR17): Novosibirsk, Russia*. 2017. [arXiv:1705.10838 \[physics.ins-det\]](https://arxiv.org/abs/1705.10838).  
<http://inspirehep.net/record/1601898/files/arXiv:1705.10838.pdf>.
- [18] A. Irles, *Latest R&D news and beam test performance of the highly granular SiW-ECAL technological prototype for the ILC*, in *proceeding of the International Conference on Calorimetry for the High Energy Frontier (CHEF 2017)*. 2017.
- [19] G. B. et.al., *Conception and construction of a technological prototype of a high-granularity digital hadronic calorimeter*, *JINST* **10** (2015) P10039.

- [20] M. B. *et al.*, *Performance of Glass Resistive Plate Chambers for a high granularity semi-digital calorimeter*, JINST **6** (2011) P02001.
- [21] C. Collaboration, *First results of the CALICE SDHCAL technological prototype*, JINST **11** (2016) P04001.
- [22] C. Collaboration, *Separation of nearby hadronic showers in the CALICE SDHCAL prototype detector using ArborPFA*, CAN-054 (2016) .
- [23] C. Collaboration, *Tracking within Hadronic Showers in the CALICE SDHCAL prototype using a Hough Transform Technique*, JINST **12** (2017) P05009.
- [24] C. Collaboration, *Resistive Plate Chamber Digitization in a Hadronic Shower Environment*, JINST **11** (2016) P06014.
- [25] L. Caponetto *et al.*, *First test of a power-pulsed electronics system on a GReP detector in a 3-Tesla magnetic field*, JINST **7** (2012) P04009.
- [26] R. Wigmans, *Calorimetry, Energy Measurement in Particle Physics*, vol. 168 (second edition). International Series of Monographs on Physics, Oxford University Press, 2017.
- [27] All publications and other results obtained in the context of the RD52 project can be found at the website(s): <http://www.phys.ttu.edu/> dream or <http://dream.knu.ac.kr>.
- [28] C. Patrignani *et al.* (Particle Data Group) [Chin. Phys. C](#) **40** (2016) 479–482.
- [29] D. E. Groom, *Energy flow in a hadronic cascade: Application to hadron calorimetry*, Nucl. Instrum. Methods A **572** (2007) 633–653.
- [30] D. E. Groom, *Erratum to "Energy flow in a hadronic cascade: Application to hadron calorimetry" [Nucl. Instr. and Meth. A 572 (2007) 633–653]*, Nucl. Instrum. Methods A **593** (2008) 638.
- [31] N. Akchurin *et al.*, *Particle identification in the longitudinally unsegmented RD52 calorimeter*, Nucl. Instrum. Methods A **735** (2014) 120.
- [32] N. Akchurin *et al.*, *The electromagnetic performance of the RD52 fiber calorimeter*, Nucl. Instrum. Methods A **735** (2014) 130.
- [33] N. Akchurin *et al.*, *Lessons from Monte Carlo simulations of the performance of a dual-readout fiber calorimeter*, Nucl. Instrum. Methods A **762** (2014) 100.
- [34] C. Cardini *et al.*, *The small-angle performance of a dual-readout fiber calorimeter*, Nucl. Instrum. Methods A **808** (2016) 41.
- [35] R. Wigmans, *New results from the RD52 project*, Nucl. Instrum. Methods A **824** (2016) 721.
- [36] S. Lee *et al.*, *Hadron detection with a dual-readout fiber calorimeter*, Nucl. Instrum. Methods A **866** (2017) 76.
- [37] 4th Detector Collaboration Letter of Intent: <http://www.4thconcept.org/4LoI.pdf>.
- [38] D. Acosta *et al.*, *Electron, pion and multiparticle detection with a lead/scintillating-fiber calorimeter*, Nucl. Instrum. Methods A **306** (1991) 481.

- [39] *10th International Conference on Calorimetry in High Energy Physics (CALOR 2002), Pasadena, California, 25-30 Mar 2002.* March, 2002.